


## Microbunch rotation in an x-ray free-electron laser using a first-order achromatic bend

Rachel A. Margraf<sup>ⓧ,\*</sup>, James P. MacArthur, Gabriel Marcus<sup>ⓧ</sup>, Heinz-Dieter Nuhn<sup>ⓧ</sup>,  
Alberto Lutman<sup>ⓧ</sup>, Aliaksei Halavanau<sup>ⓧ</sup>, Zhen Zhang<sup>ⓧ</sup>, and Zhirong Huang<sup>ⓧ†</sup>

SLAC National Accelerator Laboratory, Menlo Park, USA

 (Received 2 October 2023; accepted 29 January 2024; published 5 March 2024; corrected 21 August 2024)

Electrons in an x-ray free electron laser (XFEL) develop periodic density fluctuations, known as microbunches, which enable the exponential gain of x-ray power in an XFEL. When an electron beam microbunched at a hard x-ray wavelength is kicked, microbunches are often washed out due to the dispersion and  $R_{56}$  of the bend. An achromatic (dispersion-free) bend with a small  $R_{56}$ , however, can preserve microbunches, which rotate to follow the new trajectory of the electron bunch. Rotated microbunches can subsequently interact in a repointed undulator to produce a new beam of off-axis x rays. In this work, we demonstrate hard x-ray multiplexing in the Linac Coherent Light Source hard x-ray undulator line using microbunch rotation through a 10  $\mu$ rad first-order-achromatic bend created by transversely offsetting quadrupole magnets in the FODO lattice. Quadrupole offsets are determined analytically from beam-matrix theory. We also discuss the application of microbunch rotation to out-coupling a cavity-based XFEL.

DOI: [10.1103/PhysRevAccelBeams.27.030702](https://doi.org/10.1103/PhysRevAccelBeams.27.030702)

### I. INTRODUCTION

Since their invention, free-electron lasers (FELs) have become indispensable scientific instruments, especially when very high-power and/or very short-wavelength coherent radiations are desirable. The most essential process of the FEL is the formation of microbunches in electron beams, which is a periodic modulation of the electron density at the radiation wavelength. In a single-pass, high-gain FEL, the formation of microbunches generates coherent radiation that leads to stronger microbunching. The feedback mechanism sets up an exponential growth of the radiation power until saturation. The radiation is the most useful product of FELs. Nevertheless, microbunched electron beams are also very interesting on their own and can be manipulated for various applications. Our paper describes an approach and experimental tests of a method of manipulating these microbunches called microbunch rotation.

Microbunch rotation using achromatic bends has long been an option for out-coupling infrared FEL oscillators [1]

and has also been proposed for preserving EUV microbunches in ring FELs [2] and energy-recovery linac-based FELs [3]. Techniques under the development for steady state microbunching in a storage ring, recently demonstrated for IR wavelengths, also often minimize the dispersion and  $R_{56}$  [4,5]. However, demonstrations of microbunch rotation in the x-ray regime have been more recent.

Microbunch rotation can be achieved for soft x rays without achromatic bends. A microbunched beam kicked by an offset quadrupole develops tilted microbunches as a result of quadrupole focusing. This was observed in the commissioning of the LCLS delta undulator [6] then built upon by MacArthur *et al.* [7]. MacArthur *et al.* described the evolution of tilted microbunches following an offset quadrupole using Klimontovich distribution functions then demonstrated a 55  $\mu$ rad rotation for microbunches producing 530 eV photons [7].

However, microbunch rotation at hard x-ray spacing requires a more complicated setup to preserve microbunches. Shorter microbunches, separated at the radiation wavelength  $\lambda_r$ , are more sensitive to bunching factor degradation due to changes in the  $z$  position of the particles relative to the center of the microbunch. Cavity-based XFELs, such as the x-ray regenerative amplifier FEL [8,9] and x-ray FEL oscillator [10] typically operate Bragg-reflecting cavities at hard x-ray wavelengths. To extend microbunch rotation as an out-coupling mechanism for these cavities, we need to extend it to hard x-rays, such as the 9.832 keV x-ray energy used by the CBXFEL project [11,12]. Here we describe the theory for a first-order

\*rmargraf@stanford.edu

Also at Stanford University, Stanford, USA.

†zrh@stanford.edu

Also at Stanford University, Stanford, USA.

Published by the American Physical Society under the terms of the *Creative Commons Attribution 4.0 International* license. Further distribution of this work must maintain attribution to the author(s) and the published article's title, journal citation, and DOI.

achromatic bend of three offset quadrupole magnets and demonstrate this setup in simulation and experiments at the LCLS.

## II. THEORY

### A. Microbunch rotation by offset thin quadrupole

Microbunch rotation arises naturally from beam-matrix theory when quadrupole effects are included. We begin by defining a thin quadrupole in 4D phase space  $(y, y', z, \delta)$ , where  $y$  is a transverse coordinate,  $y' = \frac{dy}{ds}$ ,  $z$  is longitudinal along the beam axis, and  $\delta = \frac{\Delta v}{v}$ , where  $\gamma$  is the relativistic  $\gamma$ . We use the sign convention, where  $+z$  is the beam head,  $-z =$  beam tail. The quadrupole has focal length  $f$  and is offset in  $y$  by a distance  $o_1$ , producing a kick  $\theta = -\frac{1}{f}(y_0 - o_1)$ , where  $y_0$  is the transverse beam position before the quadrupole. We treat a thin offset quadrupole as an on-axis quadrupole, which also rotates the coordinate system in the  $y$ - $z$  plane by  $\theta$  to follow the beam trajectory, derived in Appendix A2. We define our initial microbunch size and divergence in the center of the quadrupole, where the focusing is at a waist ( $y$  and  $y'$  are uncorrelated), and thus specify an offset quadrupole matrix with double the focal length of our full quadrupole. For a small kick angle ( $\sin(\theta) \approx \theta$ ,  $\cos(\theta) \approx 1$ ), and microbunches that are much thinner in  $z$  than in  $y$ :

$$R_{Q\theta} = \begin{bmatrix} 1 & 0 & 0 & 0 \\ \frac{-1}{2f} & 1 & 0 & \theta \\ -\theta & 0 & 1 & 0 \\ 0 & 0 & 0 & 1 \end{bmatrix}. \quad (1)$$

We apply a drift of length  $L$  to get our final transfer matrix:

$$R = R_L R_{Q\theta} = \begin{bmatrix} 1 - \frac{L}{2f} & L & 0 & L\theta \\ \frac{-1}{2f} & 1 & 0 & \theta \\ -\theta & 0 & 1 & 0 \\ 0 & 0 & 0 & 1 \end{bmatrix}. \quad (2)$$

We assume a single Gaussian microbunch, with a sigma matrix that is uncorrelated in the center of the quadrupole:

$$\Sigma_0 = \begin{bmatrix} \sigma_{y_0}^2 & 0 & 0 & 0 \\ 0 & \sigma_{y'_0}^2 & 0 & 0 \\ 0 & 0 & \sigma_{z_0}^2 & 0 \\ 0 & 0 & 0 & \sigma_{\delta_0}^2 \end{bmatrix}. \quad (3)$$

We then evolve the microbunch envelope using the transfer matrix and obtain the second moments:

$$\Sigma = R \Sigma_0 R^T, \quad (4)$$

$$\begin{aligned} \langle y^2 \rangle &= \left(1 - \frac{L}{2f}\right)^2 \sigma_{y_0}^2 + L^2 \sigma_{y'_0}^2 + L^2 \theta^2 \sigma_{\delta_0}^2, \\ \langle z^2 \rangle &= \sigma_{z_0}^2 + \theta^2 \sigma_{y_0}^2, \\ \langle yz \rangle &= -\left(1 - \frac{L}{2f}\right) \theta \sigma_{y_0}^2. \end{aligned} \quad (5)$$

The tilt in the rotated coordinate system  $t_{yz}$  can then be geometrically found from

$$\tan(2t_{yz}) = \frac{2\langle yz \rangle}{\langle y^2 \rangle - \langle z^2 \rangle}, \quad (6)$$

$$t_{yz} \approx \frac{\langle yz \rangle}{\langle y^2 \rangle - \langle z^2 \rangle}. \quad (7)$$

In the limit of pancake microbunches,  $\langle z^2 \rangle \ll \langle y^2 \rangle$  and small kick ( $|\theta| \ll \frac{\sigma_{y_0}}{\sigma_{\delta_0}}$  and  $|\theta| \ll \frac{\sigma_{y'_0}}{\sigma_{\delta_0}}$ ), we write the tilt in terms of the beta function  $\beta_0 = \sigma_{y_0}^2 \epsilon_y = \frac{\epsilon_y}{\sigma_{y'_0}^2}$  at the waist in the center of the quadrupole:

$$t_{yz} \approx \frac{\langle yz \rangle}{\langle y^2 \rangle} = \frac{-(1 - \frac{L}{2f})\theta}{(1 - \frac{L}{2f})^2 + \frac{L^2}{\beta_0^2}}. \quad (8)$$

Equation (8) is useful for building intuition that the microbunch rotation direction is determined by the sign of  $f$ . Differentiating Eq. (8), we find

$$\left. \frac{\partial t_{yz}}{\partial L} \right|_{L=0} \approx -\frac{\theta}{2f}. \quad (9)$$

This result shows that a defocusing quadrupole ( $f < 0$ ) will rotate the microbunch in the direction of the kick  $\theta$ . With a single offset quadrupole kick, the microbunch angle will evolve continuously with drift. The next section will discuss how with additional quadrupole kicks we can create bends that instead lock the microbunch angle into the new electron trajectory.

### B. Microbunch rotation by thin quadrupole triplet

Next, we want to analyze the rotation of a microbunch through three offset quadrupoles with focal lengths  $f_1, f_2, f_3$ ; offset in  $y$  from a perfectly straight trajectory by distances  $o_1, o_2, o_3$ ; separated by drifts  $L_1, L_2$ ; and followed by a drift  $L_3$ , as shown in Fig. 1. Subsequent discussion will consider a defocusing-focusing-defocusing triplet,  $f_1 < 0, f_2 > 0, f_3 < 0$ , as this triplet achieves a given rotation with the smallest kick angles, but the analytical method can be applied to quadrupoles of arbitrary focal length.

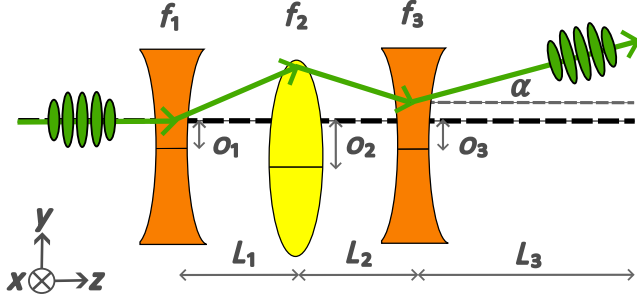


FIG. 1. Offset quadrupole triplet for microbunch rotation.

We define the transfer matrix for each offset quadrupole:

$$R_{Q\theta 1} = \begin{bmatrix} 1 & 0 & 0 & 0 \\ \frac{-1}{2f_1} & 1 & 0 & \theta_1 \\ -\theta_1 & 0 & 1 & 0 \\ 0 & 0 & 0 & 1 \end{bmatrix},$$

$$R_{Q\theta 2,3} = \begin{bmatrix} 1 & 0 & 0 & 0 \\ \frac{-1}{f_{2,3}} & 1 & 0 & \theta_{2,3} \\ -\theta_{2,3} & 0 & 1 & 0 \\ 0 & 0 & 0 & 1 \end{bmatrix}. \quad (10)$$

The kick angles can be readily solved using a matrix method, as shown in Appendix B. If  $\langle y_0 \rangle = \langle y'_0 \rangle = 0$ , the kick angles are

$$\theta_1 = \frac{o_1}{f_1},$$

$$\theta_2 = \frac{1}{f_1 f_2} (f_1 o_2 - L_1 o_1),$$

$$\theta_3 = -\frac{1}{f_1 f_2 f_3} (-f_1 f_2 o_3 + f_1 L_2 o_2 + f_2 L_2 o_1 + f_2 L_1 o_1 - L_1 L_2 o_1). \quad (11)$$

To better model the microbunch recovery, we also include a drift  $R_{56}$  term  $\frac{L}{\gamma^2}$  which we had previously neglected. When we refer to  $R_{56}$  and other matrix elements in this text, we will follow the convention to number elements based on the full 6D phase space,  $(x, x', y, y', z, \delta)$  but will write matrices in 4D phase space  $(y, y', z, \delta)$  for compactness. The drift  $R_{56}$  term accounts for particles with different energies spreading out in  $z$  due to small velocity differences over a long drift and can be significant when modeling angstrom-scale microbunches. The drift matrices are then of the form:

$$R_L = \begin{bmatrix} 1 & L & 0 & 0 \\ 0 & 1 & 0 & 0 \\ 0 & 0 & 1 & \frac{L}{\gamma^2} \\ 0 & 0 & 0 & 1 \end{bmatrix}. \quad (12)$$

Thus we can now build our transfer matrix:

$$R = R_{L3} R_{Q\theta 3} R_{L2} R_{Q\theta 2} R_{L1} R_{Q\theta 1}. \quad (13)$$

To find the tilt, one can propagate a sigma matrix defined at the center of the first quadrupole  $\Sigma_0$  through this transfer matrix using Eq. (4). An analytical expression for the microbunch tilt can be obtained using Eq. (7).

For arbitrary quadrupole offsets, the microbunch tilt will continue to evolve with additional drift distance  $L_3$ . To lock the microbunch tilt into the direction of beam travel, we need to choose offsets that satisfy  $t_{yz} = 0$  and  $\frac{\partial t_{yz}}{\partial L_3} = 0$ . This is equivalent to requiring the matrix be achromatic, e.g.,  $D = 0$  and  $D' = 0$ .  $D$  and  $D'$  are the dispersion and change in dispersion ( $R_{36}$  and  $R_{46}$ ), read directly from the transfer matrix. We also require that the sum of the trajectory kicks equals the microbunch rotation angle  $\alpha$ . Thus we solve this system of equations:

$$\begin{aligned} D &= 0, \\ D' &= 0, \\ \alpha &= \theta_1 + \theta_2 + \theta_3. \end{aligned} \quad (14)$$

Solving these equations gives us the ideal  $y$  offsets of the quadrupoles relative to the initial  $z$  axis:

$$\begin{aligned} o_1 &= \frac{\alpha f_1 f_2}{L_1}, \\ o_2 &= \frac{-\alpha f_2 (f_2 L_1 + f_2 L_2 - 2L_1 L_2)}{L_1 L_2}, \\ o_3 &= \frac{\alpha (L_2^2 + f_2 f_3)}{L_2}. \end{aligned} \quad (15)$$

If we implement microbunch rotation in a FODO lattice, where  $f_1 = f_3 = -f_2$ , and  $L_1 = L_2 = L$ , these simplify to

$$\begin{aligned} o_1 &= \frac{-\alpha f_1^2}{L}, \\ o_2 &= -2\alpha f_1 \left(1 + \frac{f_1}{L}\right), \\ o_3 &= \frac{-\alpha (f_1^2 - L^2)}{L}. \end{aligned} \quad (16)$$

The next largest factor contributing to microbunch degradation in a bend is the coupling between the energy spread and longitudinal spatial dimension, the  $R_{56}$ . If we could create an isochronous bend, where  $D = 0$ ,  $D' = 0$ , and  $R_{56} = 0$ , we could preserve all microbunching to first order, however, this condition requires strong quadrupole focusing and is much more difficult to achieve. Thus we do not pursue an isochronous bend but optimize our lattice

such that the  $R_{56}$  is small. For an offset quadrupole triplet in a FODO lattice,  $R_{56}$  is

$$R_{56} = \alpha^2 f_1 \left( 1 + \frac{2f_1}{L} \right) + \frac{2L}{\gamma^2}. \quad (17)$$

Figure 2 shows an example of tracking  $D$ ,  $D'$ , and  $R_{56}$  through an offset quadrupole triplet, for a 10  $\mu\text{rad}$  rotation with the parameters given in Table I, experiment I ( $f_1 = -12$  m). The term in Eq. (17) proportional to  $\alpha^2$  gives the  $R_{56}$  caused by the kick in the dispersive region in the center of the quadrupole [ $R_{56} = \int_0^{L_{\text{full}}} h(s)D(s)ds$ , where  $h(s)$  is the orbit curvature]. The remaining  $R_{56}$  comes from the drift  $R_{56}$  and develops smoothly through each drift. In hard XFEL regimes, the drift  $R_{56}$  can often be larger than, or comparable to, the  $R_{56}$  produced by the quadrupole kicks. We can then obtain an analytical estimate of the microbunch recovery through an offset quadrupole triplet in a FODO lattice. We consider a Gaussian microbunch with no initial longitudinal energy correlation ( $\sigma_{z,\delta} = 0$ ) with an initial bunching factor:

$$b_0 = e^{-\frac{1}{2} \left( \frac{2\alpha}{\lambda_r} \right)^2 \sigma_{z_0}^2}. \quad (18)$$

Using the  $\Sigma$  matrix method given in Eq. (4), we can evolve this microbunch through our achromatic bend and find that

$$\sigma_z^2 = \sigma_{z_0}^2 + R_{56}^2 \sigma_{\delta_0}^2. \quad (19)$$

Equation (19) remains true even if  $\langle yy' \rangle$  terms are present in the  $\Sigma_0$  matrix. The microbunch recovery for ideal Gaussian microbunches with no initial energy correlation is thus

$$\begin{aligned} \frac{b}{b_0} &= e^{-\frac{1}{2} \left( \frac{2\alpha}{\lambda_r} \right)^2 (\sigma_z^2 - \sigma_{z_0}^2)} \\ &= e^{-\frac{1}{2} \left( \frac{2\alpha}{\lambda_r} \right)^2 (R_{56}^2 \sigma_{\delta_0}^2)} \\ &= e^{-\frac{1}{2} \left( \frac{2\alpha}{\lambda_r} \right)^2 \left[ \alpha^4 f_1^2 \left( \frac{4f_1^2}{L^2} + \frac{4f_1}{L} + 1 \right) + \frac{4\alpha^2 f_1}{\gamma^2} (2f_1 + L) + \frac{4L^2}{\gamma^4} \right] \sigma_{\delta_0}^2}. \end{aligned} \quad (20)$$

The  $R_{56}$ , microbunching wavelength, and electron energy spread thus set a limit on the bunching recovery through the achromat.

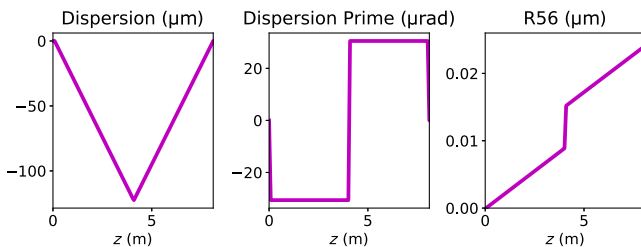


FIG. 2. Key matrix parameters for a 10  $\mu\text{rad}$  rotation with the parameters given in Table I, experiment I.

### C. Microbunch rotation by a semithick quadrupole

We also pursued a semithick lens approach, where we treat the transverse focusing in the  $y - y'$  plane as a thick quadrupole but treat the kick as instantaneous (see Appendix A3 for derivation). We consider a quadrupole with length  $l_Q$  and  $k^2 = \frac{B'e}{p} = \frac{1}{|f|l_Q}$ , where  $p$  is the electron momentum and  $e$  is the electron charge. A thick offset defocusing or focusing quadrupole that provides an instantaneous kick can be defined, respectively:

$$\begin{aligned} R_{Q_D\theta} &= \begin{bmatrix} \cosh(kl_Q) & \frac{1}{k} \sinh(kl_Q) & 0 & 0 \\ k \sinh(kl_Q) & \cosh(kl_Q) & 0 & \theta \\ -\theta & 0 & 1 & \frac{l_Q}{\gamma^2} \\ 0 & 0 & 0 & 1 \end{bmatrix}, \\ R_{Q_F\theta} &= \begin{bmatrix} \cos(kl_Q) & \frac{1}{k} \sin(kl_Q) & 0 & 0 \\ -k \sin(kl_Q) & \cos(kl_Q) & 0 & \theta \\ -\theta & 0 & 1 & \frac{l_Q}{\gamma^2} \\ 0 & 0 & 0 & 1 \end{bmatrix}. \end{aligned} \quad (21)$$

For the defocusing-focusing-defocusing case, we again build our transfer matrix similar to Eq. (13), shortening  $l_Q$  by half in the first quadrupole and using the full  $l_Q$  in the second two.  $\theta_1$ ,  $\theta_2$ , and  $\theta_3$  are also recalculated using thick quadrupoles. We solve for the optimal offsets using the system of equations in Eq. (14), obtaining a lengthy analytical solution for the optimal offsets which we applied to our subsequent experimental and simulated setups (see Supplemental Material [13]).

Figure 3 shows the microbunch recovery through a triplet for a single Gaussian microbunch for this analytical model with the parameters given in Table I, experiment I, and two

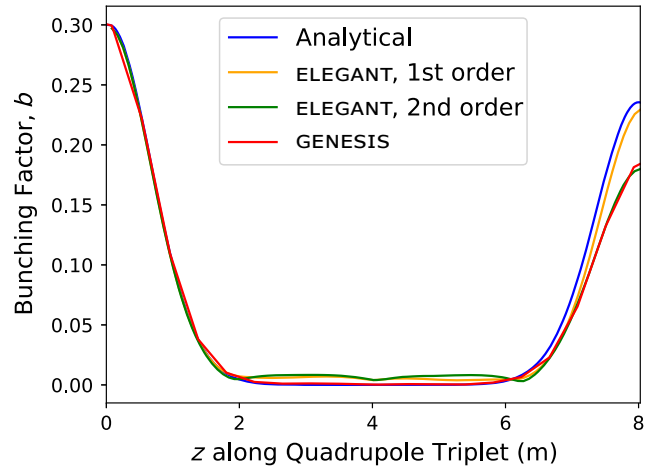


FIG. 3. Bunching factor through a microbunch rotation triplet, using the parameters in Table I, experiment I, 10  $\mu\text{rad}$ . The bunching factor is compared for the analytical model with thick quadrupoles, ELEGANT with first- or second-order matrices, and GENESIS.

TABLE I. Experimental parameters.

$B'_1 l_Q = B'_3 l_Q, -B'_2 l_Q$		$(-3, 3)$ T	$L_1 = L_2$	4.013 m	
$l_Q$		8.4 cm	$\lambda_u, n_{\lambda_u}$	2.6 cm, 130	
<hr/>					
Experiment I					
$E_{e^-}$	10.79 GeV		$E_{\lambda_r}$	10.14 keV	
$\epsilon_{x,\text{norm}}$	$0.4 \times 10^{-6}$ mrad <sup>a</sup>		$I_{\text{core}}$	4.4 kA	
$\Delta t_{\text{FWHM}}$	33 fs		$\Delta E_{\text{slice}}$	5.0 MeV	
<hr/>					
$o_{1,10 \mu\text{rad}}$	366 $\mu\text{m}$	$o_{2,10 \mu\text{rad}}$	489 $\mu\text{m}$	$o_{3,10 \mu\text{rad}}$	323 $\mu\text{m}$
$o_{1,20 \mu\text{rad}}$	733 $\mu\text{m}$	$o_{2,20 \mu\text{rad}}$	978 $\mu\text{m}$	$o_{3,20 \mu\text{rad}}$	646 $\mu\text{m}$
<hr/>					
Experiment II					
$E_{e^-}$	11.42 GeV		$E_{\lambda_r}$	11.3 keV	
$\epsilon_{x,\text{norm}}$	$0.4 \times 10^{-6}$ mrad <sup>a</sup>		$I_{\text{core}}$	3.4 kA	
$\Delta t_{\text{FWHM}}$	45 fs		$\Delta E_{\text{slice}}$	< 13.2 MeV <sup>b</sup>	
<hr/>					
$o_{1,10 \mu\text{rad}}$	410 $\mu\text{m}$	$o_{2,10 \mu\text{rad}}$	563 $\mu\text{m}$	$o_{3,10 \mu\text{rad}}$	367 $\mu\text{m}$

<sup>a</sup>Typical LCLS value.<sup>b</sup>Measured while lasing not fully suppressed.

simulation software programs, ELEGANT [14] and GENESIS 1.3 [15,16]. ELEGANT can perform electron beam transport using first- or second-order matrices. We find the analytical model gives a result close to ELEGANT's when we only consider first-order effects. The microbunch recovery is then decreased when the second-order effects are included, as consistently shown in ELEGANT and GENESIS [13].

### III. WORKABLE REGIMES FOR MICROBUNCH ROTATION

The preservation of microbunches following microbunch rotation in an achromatic bend depends strongly on the properties of the bend, bunching, and electron beam. To first order, the microbunch recovery can be described using Eq. (20), where the microbunch recovery depends on the microbunch wavelength (or equivalently, photon energy), electron beam energy spread, electron beam energy, quadrupole strength, and the drift distances between the quadrupoles. Figure 4 shows the variation in microbunch recovery for the conditions in experiment I as each of these parameters is scanned, and the quadrupole offsets were updated accordingly. Here we use the experiment I parameters given in Table I, except for the initial energy spread, where we use 6.1 MeV instead of 5 MeV to account for the increase in energy spread from the beginning of the undulator hall to the microbunch rotation triplet. The analytical curve represents Eq. (20), and the datapoints represent simplified GENESIS simulations, where a single Gaussian microbunch is transported through an offset quadrupole triplet.

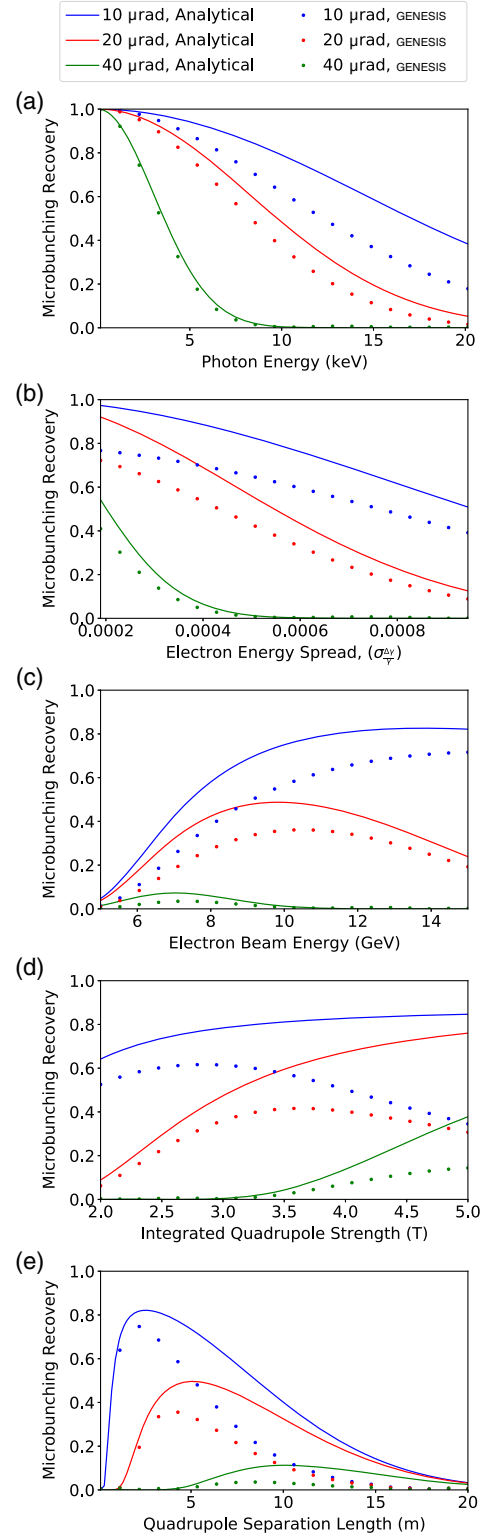


FIG. 4. Microbunch recovery as a function of (a) photon energy, (b) electron beam energy spread, (c) electron beam energy, (d) quadrupole strength, and (e) the drift distance between quadrupoles. Parameters in Table I, experiment I, were used.

Microbunch recovery is highest for long-wavelength microbunches (low photon energies) and low energy spread, which minimize the impact of the  $R_{56}$ . The other three parameters are optimized by minimizing the  $R_{56}$ . The electron beam energy and quadrupole strength both determine the quadrupole focal length (for thin quadrupoles,  $f = \frac{p}{B'l_Q e}$ ). Higher electron energy increases the quadrupole focal length but reduces the drift  $R_{56}$ , leading to an optimum which can be approximated numerically from Eq. (17).

For the quadrupole strength, one can derive Eq. (17) to find the minimum  $R_{56}$  occurs around  $f_1 = -\frac{L}{4}$ , giving an optimal quadrupole strength of  $B'l_Q = -\frac{4p}{Le}$ , which predicts an optimal value of  $B'l_Q = -36$  T. Thus to first order, stronger quadrupoles provide better microbunch recovery.

Deriving Eq. (17) with respect to  $L$ , we find the optimal quadrupole separation is approximately  $L = |\alpha f_1 \gamma|$ , which for a  $10 \mu\text{rad}$  rotation is approximately 2.5 m. This represents a trade-off between a stronger second quadrupole kick in the dispersive region for a shorter drift distance and a longer drift distance causing the drift  $R_{56}$  to degrade the microbunching.

Second-order effects can reduce the actual microbunch recovery from these analytical estimates, particularly in the regime of strong quadrupole focusing, thus Eq. (20) is only approximate. Equation (20) and the simulations shown here also only consider a Gaussian microbunch with no initial  $z\delta$  correlation. Microbunches in an FEL, by contrast, have  $z\delta$  correlation, and this can cause bunching factor enhancement for a small  $R_{56}$ . Thus we can improve the microbunch recovery by performing microbunch rotation before FEL saturation.

#### IV. EXPERIMENTAL DEMONSTRATION OF MICROBUNCH ROTATION

##### A. Setup

We performed two microbunch rotation experiments using the Cu LCLS linac with the upgraded LCLS-II hard x-ray undulator (HXU) line [17] between April and June 2021. Figure 5 shows the experimental setup. Each HXU undulator and its associated quadrupole can be moved transversely  $\pm 1$  mm. We used this girder motion in  $y$  to form our offset quadrupole triplet and open-gapped the two

undulators in the center of our triplet. We lased in 21 on-axis undulators, performed microbunch rotation, then repointed the remaining 9 undulators by  $10$  or  $20 \mu\text{rad}$ . In doing so, we note that the electron beam does not return on axis in the third quadrupole but returns to a position of approximately  $\alpha L$ . An example trajectory is shown in Fig. 21.

Experimental parameters are given in Table I.  $B'l_Q$ ,  $B'l_Q$ , and  $B'l_Q$  are the integrated quadrupole gradients,  $l_Q$  is the effective quadrupole length,  $\lambda_u$  is the undulator period, and  $n_{\lambda_u}$  is the number of periods per undulator.  $E_{e^-}$  and  $E_{\lambda_r}$  define the energy of the electron and x-ray beams.  $\epsilon_{x,\text{norm}}$  is a typical LCLS Cu linac normalized emittance in the undulator line.  $\Delta t_{\text{FWHM}}$ ,  $I_{\text{core}}$ , and  $\Delta E_{\text{slice}}$  define the FWHM electron beam pulse duration, the average current, and the average rms slice energy spread within the central FWHM pulse duration. These last three quantities were calculated from measured time-resolved energy distribution of the electron bunch downstream of the undulator line. Time dependent horizontal streaking is provided by an XTCAV [18]. For experiment I, these quantities were measured without undulator lasing, giving a reliable measurement of the energy spread, while for experiment II, FEL lasing was only partially suppressed, and thus we can only set an upper limit on the energy spread. The XTCAV measurements are shown in detail in Appendix F.

##### B. Example images

Figure 6 shows averaged single-shot images on the downstream screen. Screen coordinates have been converted into the angular separation between the two beams to clearly show multiplexing at  $10$  and  $20 \mu\text{rad}$ . For experiment I, mean angular separations between the two rotated spots were  $(9.9 \pm 0.1) \mu\text{rad}$  and  $(20.1 \pm 0.1) \mu\text{rad}$ , respectively. For experiment II, the mean angular separation between the two rotated spots was  $(9.5 \pm 0.1) \mu\text{rad}$ . The uncertainty is given by the precision of the screen pixel size calibration. These measurements may show a slightly smaller spot separation than expected. Figure 14 shows that even in experiment I, the initial spot separation in early undulators suggests less than  $10 \mu\text{rad}$  rotation, and the good agreement only arises after gain guiding. Figure 11 shows that choosing quadrupole offsets using a thick

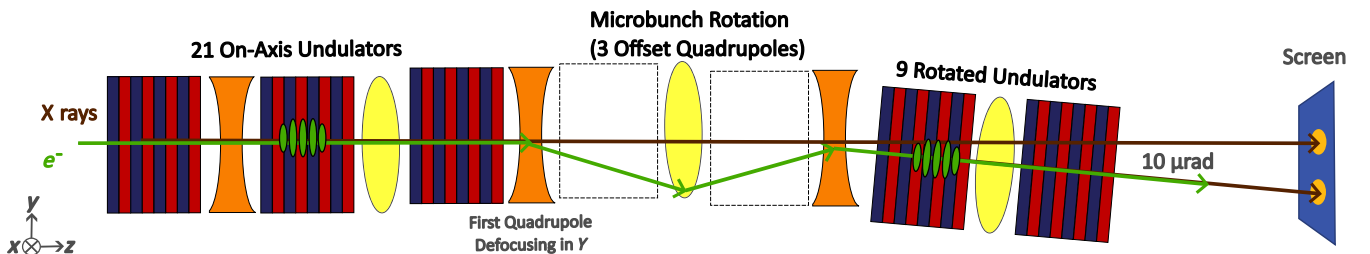


FIG. 5. Side view of experimental setup in LCLS-II hard x-ray undulator hall.

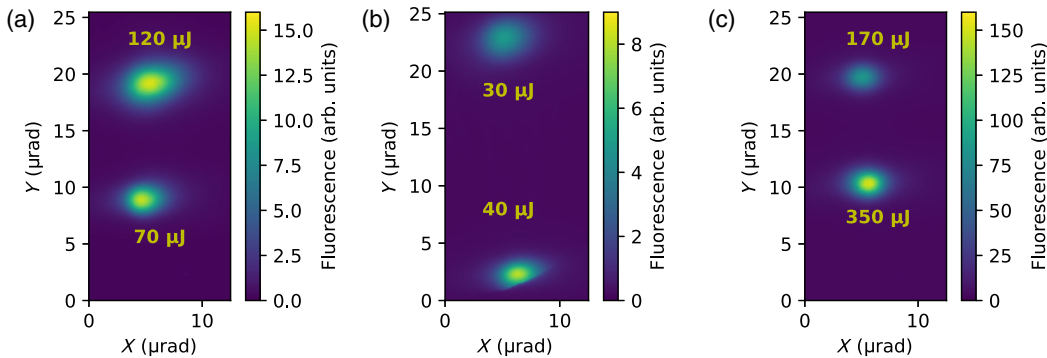


FIG. 6. Averaged images showing the on axis (top) and rotated (bottom) spots. (a) Experiment I, 10  $\mu\text{rad}$ , (b) experiment I, 20  $\mu\text{rad}$ , and (c) experiment II, 10  $\mu\text{rad}$ . Approximate spot pulse energies are given next to each spot.

quadrupole with instantaneous kick (over a full integrated function magnet) might explain the angular separation being 0.1  $\mu\text{rad}$  less than predicted. Additionally, if the electron beam might have been injected off-axis on the 10s of  $\mu\text{m}$  scale, Fig. 15 shows that a 0.5–1  $\mu\text{rad}$  deviation from the ideal angular separation may not be too surprising.

To accommodate large quadrupole offsets within the range of the undulator girder movers, the on-axis beam was repositioned between the 10 and 20  $\mu\text{rad}$  datasets. Without additional tuning, this caused lower power in the on-axis spot in the 20  $\mu\text{rad}$  case. This repositioning was additionally important to allow the 20  $\mu\text{rad}$  repositioned spot to pass through the aperture on the gas detector. Further repositioning could have prevented the rotated spot in Fig. 6(b) from being clipped by this aperture.

### C. $K$ Optimization

We maximized x-ray power by scanning  $K$  in the rotated undulator section, as shown in Fig. 7. As the electron beam transits down the undulator line, it loses energy to resistive wall wakefields. The average energy loss is compensated for by a typical LCLS early stage linear taper of  $\Delta K = -0.000185$  per undulator. In later undulators, a quadratic taper can be added to match energy loss due to the FEL process [19]. During normal LCLS operation, both linear and quadratic terms of the taper are scanned. To optimize power in the rotated section, we scanned a constant offset of the undulator  $K$  for a linear (A,D) or quadratic (B,C) taper (see Appendix C for full taper plots). These simple, single-parameter scans increased the power in the rotated spot significantly, and future studies could further optimize linear, quadratic, and higher order terms for further power extraction.

For Fig. 7(a), the average  $K$  in the undulator directly upstream of the microbunch rotation triplet was 2.5439, and the  $K$  following the linear taper for the first repositioned undulator would be 2.5431. However, when we scan the repositioned undulator section, while keeping the linear taper, we find the optimal  $K$  of the first repositioned undulator is 2.5396, a detune of  $(-0.139 \pm 0.002)\%$ .

One possible explanation for this  $K$  detune is that the tail of the electron beam was predominantly lasing in this experiment. While the linear taper matches the mean energy loss due to wakefields, the energy loss from resistive-wall wakefields is higher in the tail of the beam relative to the head. When our microbunched beam enters the rotated undulator section, the resonant bunching wavelength  $\lambda_r = \frac{\lambda_u}{2\gamma^2} (1 + \frac{K^2}{2})$  is fixed. However, in the second stage, the resonant  $K$  can change with electron beam energy loss. If the bunching is strongest in the beam tail, which loses more energy due to resistive wall wakefields than the linear taper compensates for, then a lower  $K$  will be more strongly resonant.

There are many ways that preferential lasing on the beam tail can occur during LCLS operation. One scenario is that the  $z$ - $x$  phase space of the electron beam is tilted, which can occur due to uncorrected kicks, such as from coherent synchrotron radiation, in a dispersive region. An electron beam with a large tilt will only lase in one part of the beam, as the rest of the beam undergoes an orbit in the undulator. The  $z$ - $x$  tilt is flattened during accelerator operation by adjusting quadrupoles in the dispersive BC2 region, however, it is not always optimized properly. For the GENESIS simulations shown in Fig. 7, we performed start-to-end ELEGANT simulations to produce the initial electron beam at the start of the undulator, in which we adjusted the quadrupoles in the BC2 region to add a tilt to the beam. We then injected the electron beam into the undulator with the tail of the beam on axis and matched to the quadrupole focusing lattice. The  $K$  detune can be freely adjusted in simulation by changing which part of the electron beam is matched. Figure 19 provides a demonstration of this effect. We found good agreement in the  $K$  detune by dividing the beam into 100 bins, then matching the 67th bin from the beam head for Figs. 7(a)–7(c) and the 73rd bin from the beam head for Fig. 7(d).

Comparing Figs. 7(a) and 7(b), the quadratic taper causes the detune in the first undulator to be slightly less negative, as the average  $K$  in the repositioned section is lower.

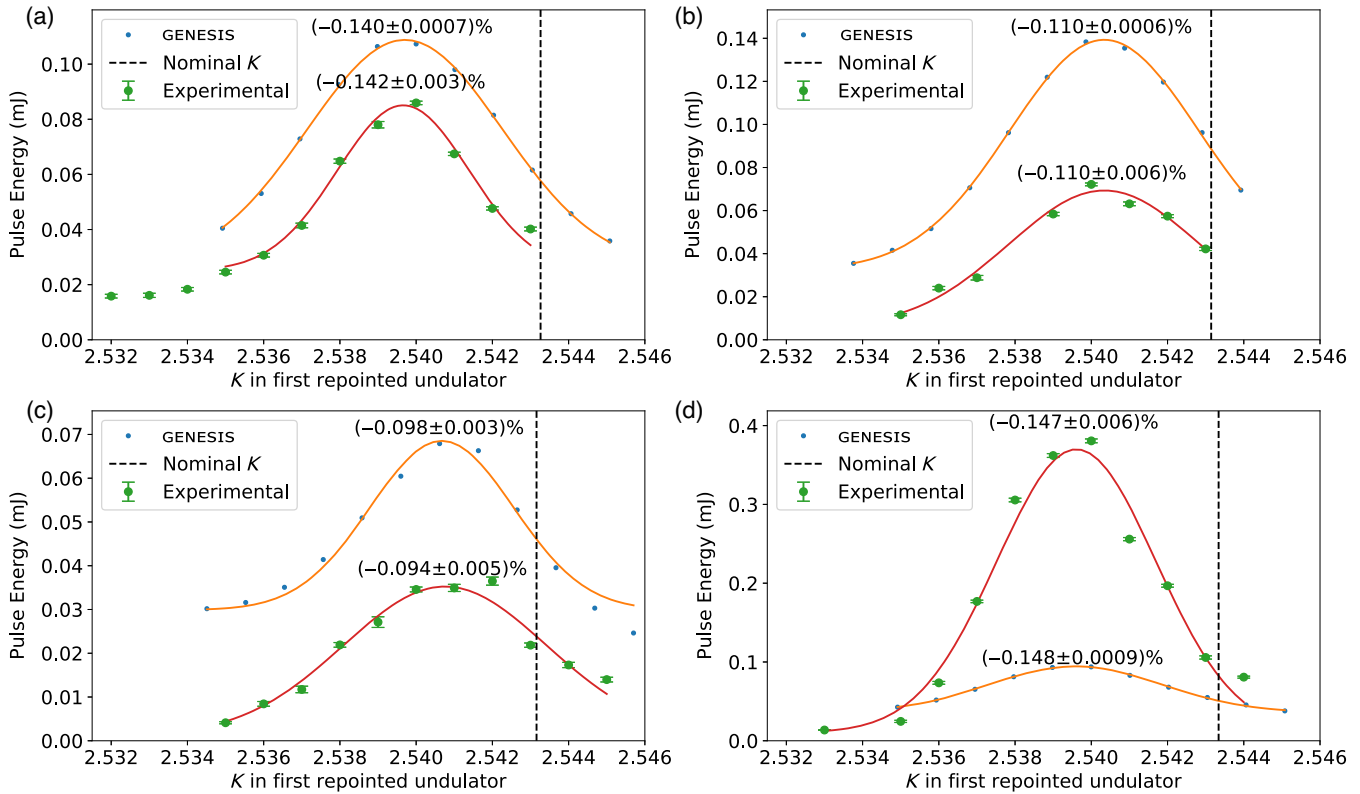


FIG. 7. Scans of the  $K$  in the reprinted undulator line for (a) experiment I,  $10\ \mu\text{rad}$ , linear taper; (b) experiment I,  $10\ \mu\text{rad}$ , quadratic taper; (c) experiment I,  $20\ \mu\text{rad}$ , quadratic taper; and (d) experiment II,  $10\ \mu\text{rad}$ , linear taper. Overlaid text gives the Gaussian-fitted  $K$  detune as a percentage of nominal  $K$ . Error bars give the standard error of the mean. Errors in fit centers give the error on the Gaussian fit.

The  $K$  detune, however, is not strongly affected by the microbunch rotation angle, as can be seen by comparing Figs. 7(b) and 7(c). This suggests that the  $K$  detune is due to energy loss in the undulator line and is not caused by the microbunch rotation process.

#### D. Gain curve

We examined the gain in the reprinted undulator section by inserting a kick after each reprinted undulator, as shown in Fig. 8, with a polynomial fit. We predicted the gain curve would be quadratic, consistent with superradiant emission [20], and our simulation results. The experimental gain appears to be primarily linear with a quadratic component. We suspect that the seventh reprinted undulator was behaving poorly during the experiment, as shown in Fig. 13, and thus further experiments might show a more quadratic gain curve.

#### E. Phaseshifter scan

To demonstrate that the gain in the reprinted undulator section comes from the microbunching in the electron beam, and not from interaction with the on-axis x-ray seed, we performed a phaseshifter scan, as shown in Fig. 9. In a typical on-axis undulator, using a phaseshifter to delay

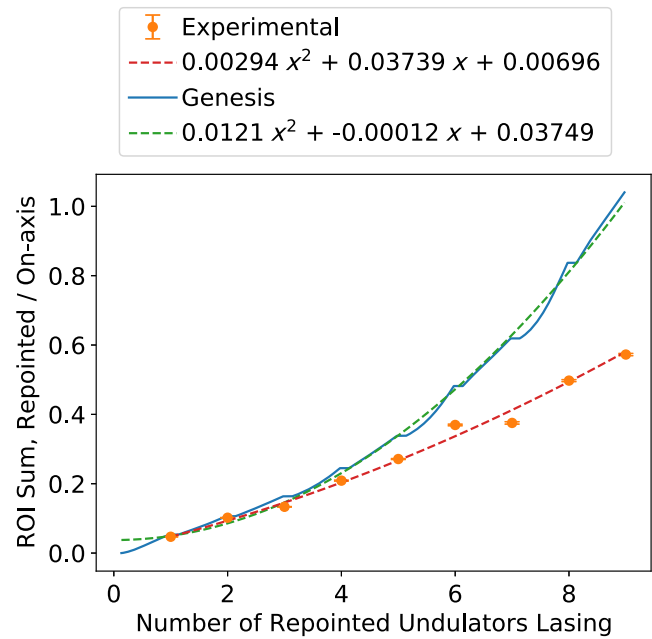


FIG. 8. Gain in rotated undulator section for the  $10\ \mu\text{rad}$ , experiment I, quadratic taper case. In this run, the power in the on-axis spot was  $120\ \mu\text{J}$ . Error bars give the standard error of the mean.



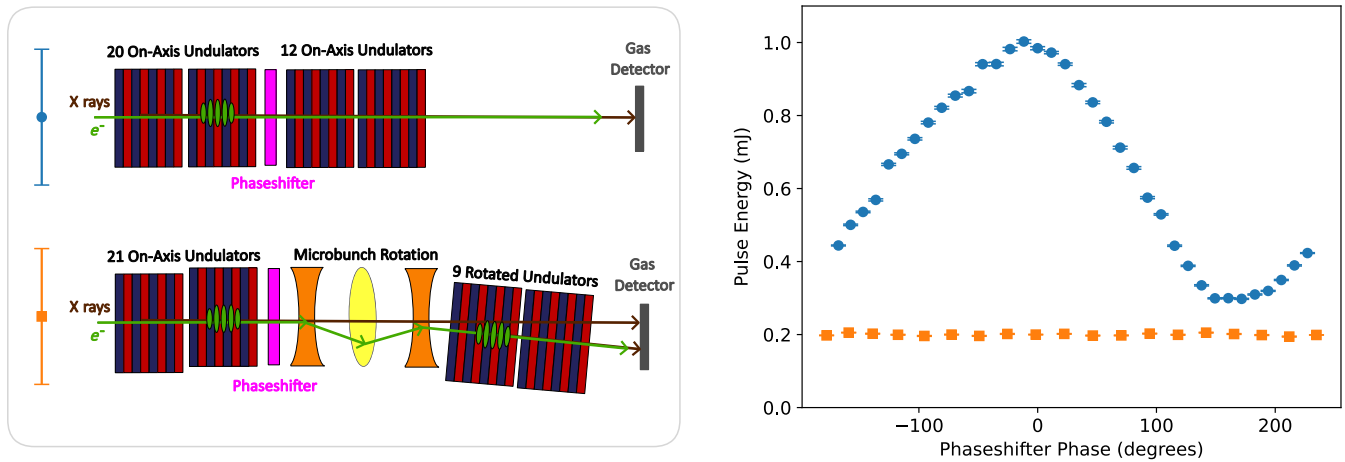


FIG. 9. Phaseshifter scan demonstration for experiment I,  $10 \mu\text{rad}$  case. With all 32 undulators aligned on axis, a phaseshifter was scanned (blue circles). With the microbunch rotation triplet and reprinted undulator line installed, the phaseshifter just upstream of the microbunch rotation triplet was scanned (orange squares). Error bars give the standard error of the mean.

the electron bunch by  $180^\circ$  relative to the x-ray pulse suppresses lasing. However, we find that in the microbunch rotation case, the power in the reprinted undulator section does not change. This suggests that there is a negligible interaction between the on-axis x-ray beam and the reprinted electron beam.

## V. CONCLUSIONS AND PROPOSED APPLICATIONS

These results demonstrate that the microbunch rotation is possible with hard x-ray wavelengths. To our knowledge, our demonstration is the first time microbunch rotation has been demonstrated with the hard x-ray microbunches in the literature. Furthermore, demonstrating the microbunch rotation with hard x-ray spacing at  $> 10 \mu\text{rad}$  is significant for the application of microbunch rotation to a cavity-based XFEL.

Proposed cavity-based CBXFELs [11,12,21] use Bragg-reflecting mirrors to circulate x-ray pulses which interact with a series of electron bunches. The CBXFEL project [11,12] will test a rectangular cavity of diamond

(400) Bragg-reflecting mirrors at 9.832 keV, which have an angular reflectivity bandwidth (FWHM) of  $8.8 \mu\text{rad}$ .

A microbunch rotation out-coupling scheme for a cavity-based XFEL is depicted in Fig. 10. X rays produced by on-axis undulators remain inside the cavity, while reprinted x rays miss the rocking curve of the Bragg reflection and are transmitted out of the cavity.

A  $10 \mu\text{rad}$  microbunch rotation is sufficient to miss the Bragg rocking curve of the diamond 400 reflection used by the CBXFEL project. Thus our demonstration of 10 and  $20 \mu\text{rad}$  rotation of 10.14 keV microbunches supports the feasibility of microbunch rotation for out-coupling a hard x-ray cavity.

In certain regimes, one could also preserve microbunching as the electron beam is sent around the cavity mirror, as discussed further in Appendix G.

The ability to multiplex an XFEL beam may additionally be useful for stereo imaging, in which two photon beams strike a sample simultaneously at different angles [22,23]. Upcoming LCLS-II upgrades will install a tender x-ray imaging hutch with the ability to cross x-ray beams from two separate undulator lines [17]. The two angularly

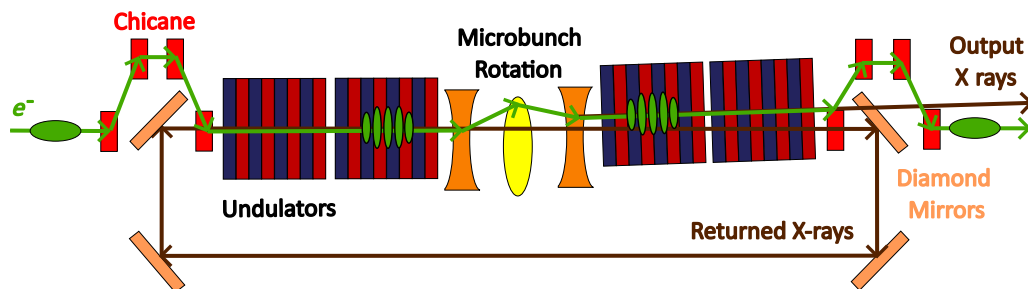


FIG. 10. Microbunch rotation as an outcoupling scheme for a cavity-based XFEL.

separated hard x-ray beams from microbunch rotation-based multiplexing could be crossed using Bragg-reflecting mirrors, potentially enabling stereo imaging with a single undulator line. Additionally, because x-rays are produced from the same microbunches, future studies could pursue producing phase-locked pulses using this method.

Our results demonstrate a simple scheme for implementing microbunch rotation for hard x-ray multiplexing in existing FEL facilities and have exciting applications for CBXFEL outcoupling and other experiments. We expect the ability to perform multiplexing with little additional hardware may be useful to existing XFEL facilities to design new operational modes and utilize the full potential of these very flexible machines.

### ACKNOWLEDGMENTS

This work was supported by the U.S. Department of Energy under Contract No. DE-AC02-76SF00515. The authors wish to thank David Cesar, Franz-Josef Decker, Xiujie Deng, Zhaoheng Guo, and Sven Reiche for insightful conversations and guidance on running GENESIS, and Timothy Maxwell for his assistance with XTCAV measurements.

## APPENDIX A: THIN, THICK, AND SEMITHICK OFFSET QUADRUPOLES

For determining the matrix to use an offset quadrupole, we can consider: (i) an integrated function magnet with both dipole and quadrupole moments, (ii) a thin offset quadrupole of infinitesimal length, or (iii) a thick quadrupole that provides an instantaneous kick. While (i) is the most accurate, (ii) and (iii) can be more tractable and provide good approximations within the appropriate limits.

### 1. Integrated function magnet

To properly account for a bend with focusing, we could use something akin to the wedge bend in Chao, Sec. 2.2, Eq. 15 [24] [reproduced for four-dimensional phase space  $(y, y', z, \delta)$ , with the sign convention  $+z =$  beam head,  $-z =$  beam tail, in Eq. (A1)]. This matrix describes a combined (integrated) function magnet applicable to an offset quadrupole, which is focusing in  $y$ . These matrices neglect the vacuum  $R_{56, \frac{l_Q}{\rho^2}}$ , but one could also add it in for completeness.

$$R_{\text{offset focusing quad}} = \begin{bmatrix} \cos(k_y l_Q) & \frac{1}{k_y} \sin(k_y l_Q) & 0 & \frac{h}{k_y^2} (1 - \cos(k_y l_Q)) \\ -k_y \sin(k_y l_Q) & \cos(k_y l_Q) & 0 & \frac{h}{k_y} \sin(k_y l_Q) \\ -\frac{h}{k_y} \sin(k_y l_Q) & -\frac{h}{k_y^2} (1 - \cos(k_y l_Q)) & 1 & -\frac{h^2}{k_y^3} (k_y l_Q - \sin(k_y l_Q)) \\ 0 & 0 & 0 & 1 \end{bmatrix}. \quad (\text{A1})$$

In this formalism,  $h = \frac{1}{\rho}$ ,  $\rho = \frac{l_Q}{\theta}$ ,  $k_y^2 = (1 - n)h^2$ , and  $n = -\frac{\partial B}{\partial y} \frac{\rho}{B}$ . Since  $k_{y,\text{quad}}^2 = \frac{B'}{B\rho}$ ,  $n = -k_{y,\text{quad}}^2 \rho^2$ , and  $k_y = \sqrt{\frac{1}{\rho^2} + k_{y,\text{quad}}^2}$ . Thus this matrix can be used for a thick offset quadrupole kick, if we know the kick angle  $\theta$  and  $k_y$  is real, as in the case of a focusing quadrupole. If  $k_y$  is imaginary, as in the case of a defocusing quadrupole ( $B' < 0$ ) and a weak bend ( $\frac{1}{\rho^2} < |k_{y,\text{quad}}^2|$ ), then we can transform Eq. (A1) using  $k_y \rightarrow ik_y$  and the identities  $\sinh(u) = -i \sin(iu)$  and  $\cosh(u) = \cos(iu)$ :

$$R_{\text{offset defocusing quad}} = \begin{bmatrix} \cosh(k_y l_Q) & \frac{1}{k_y} \sinh(k_y l_Q) & 0 & -\frac{h}{k_y^2} (1 - \cosh(k_y l_Q)) \\ k_y \sinh(k_y l_Q) & \cosh(k_y l_Q) & 0 & \frac{h}{k_y} \sinh(k_y l_Q) \\ -\frac{h}{k_y \sinh(k_y l_Q)} & \frac{h}{k_y^2} (1 - \cosh(k_y l_Q)) & 1 & \frac{h^2}{k_y^3} (k_y l_Q - \sinh(k_y l_Q)) \\ 0 & 0 & 0 & 1 \end{bmatrix}. \quad (\text{A2})$$

Using Eq. (A2), we then use  $k_y = \sqrt{|\frac{1}{\rho^2} - |k_{y,\text{quad}}^2||}$ .

### 2. Thin offset quadrupole

Let us now consider how to approximate a thin offset quadrupole. Unfortunately, neither Eq. (A1) or Eq. (A2) can be cleanly reduced to a thin bend. Consider the case with no focusing, e.g.,  $k_y = h$ ,  $n = 0$ :

$$R_{\text{uniform bend}} = \begin{bmatrix} \cos(\theta) & \frac{1}{h}\sin(\theta) & 0 & \frac{1}{h}(1 - \cos(\theta)) \\ -h\sin(\theta) & \cos(\theta) & 0 & \sin(\theta) \\ -\sin(\theta) & -\frac{1}{h}(1 - \cos(\theta)) & 1 & -\frac{1}{h}(\theta - \sin(\theta)) \\ 0 & 0 & 0 & 1 \end{bmatrix}. \quad (\text{A3})$$

Consider small kicks,  $\cos(\theta) \approx 1 - \theta^2$ ,  $\sin(\theta) \approx \theta$ , and substitute  $h = \frac{\rho}{l_Q}$ :

$$R_{\text{uniform bend}} = \begin{bmatrix} 1 - \theta^2 & l_Q & 0 & l_Q \\ -\frac{\theta^2}{l_Q} & 1 - \theta^2 & 0 & \theta \\ -\theta & -l_Q\theta & 1 & 0 \\ 0 & 0 & 0 & 1 \end{bmatrix}. \quad (\text{A4})$$

We run into trouble when we want to set  $l_Q = 0$ , where  $R_{43}$  becomes infinite. Thus we cannot reduce this expression to a matrix for an instantaneous kick.

Instead, we turn to a different method. We use a rotation matrix as a proxy for the instantaneous kick. A rotation in  $y$ - $z$  can be expressed as

$$\begin{bmatrix} y_1 \\ z_1 \end{bmatrix} = \begin{bmatrix} \cos(\theta) & \sin(\theta) \\ -\sin(\theta) & \cos(\theta) \end{bmatrix} \begin{bmatrix} y_0 \\ z_0 \end{bmatrix}. \quad (\text{A5})$$

Thus

$$\begin{aligned} y_1 &= \cos(\theta)y_0 + \sin(\theta)z_0, \\ z_1 &= -\sin(\theta)y_0 + \cos(\theta)z_0. \end{aligned} \quad (\text{A6})$$

Identifying  $y' = \frac{\partial y}{\partial s}$ ,  $z' = \frac{\partial z}{\partial s}$ , we also get

$$\begin{aligned} y'_1 &= \cos(\theta)y'_0 + \sin(\theta)z'_0, \\ z'_1 &= -\sin(\theta)y'_0 + \cos(\theta)z'_0. \end{aligned} \quad (\text{A7})$$

$$\begin{bmatrix} y_1 \\ y'_1 \\ z_1 \\ z'_1 \end{bmatrix} = \begin{bmatrix} \cos(\theta) & 0 & \sin(\theta) & 0 \\ 0 & \cos(\theta) & 0 & \sin(\theta) \\ -\sin(\theta) & 0 & \cos(\theta) & 0 \\ 0 & -\sin(\theta) & 0 & \cos(\theta) \end{bmatrix} \begin{bmatrix} y_0 \\ y'_0 \\ z_0 \\ z'_0 \end{bmatrix}. \quad (\text{A8})$$

To put this into  $(y, y', z, \delta)$  phase space, we use conservation of momentum to require  $p_1 = p_0$ ,  $\frac{p_0^2}{m^2} = y_0'^2 + z_0'^2$ , and  $\frac{p_1^2}{m^2} = y_1'^2 + z_1'^2$ . Then we find  $z_0 = \sqrt{\frac{p_0^2}{m^2} - y_0'^2}$  and solve for  $y'_1$  in terms of  $p_0$  and  $y'_0$ :

$$\begin{aligned} y'_1 &= \cos(\theta)y'_0 + \sin(\theta)\sqrt{\frac{p_0^2}{m^2} - y_0'^2} \\ &\approx \cos(\theta)y'_0 + \sin(\theta)\frac{p_0}{m}. \end{aligned} \quad (\text{A9})$$

The second approximation is made assuming  $y'_0 \ll \frac{p_0}{m}$ . Using this, we can now write the rotation matrix in  $(y, y', z, \delta)$  phase space:

$$\begin{bmatrix} y_1 \\ y'_1 \\ z_1 \\ \delta_1 \end{bmatrix} = \begin{bmatrix} \cos(\theta) & 0 & \sin(\theta) & 0 \\ 0 & \cos(\theta) & 0 & \sin(\theta) \\ -\sin(\theta) & 0 & \cos(\theta) & 0 \\ 0 & 0 & 0 & 1 \end{bmatrix} \begin{bmatrix} y_0 \\ y'_0 \\ z_0 \\ \delta_0 \end{bmatrix}. \quad (\text{A10})$$

For very small kick angles,  $\cos(\theta) \approx 1$ ,  $\sin(\theta) \approx \theta$ , this is approximately

$$\begin{bmatrix} y_1 \\ y'_1 \\ z_1 \\ \delta_1 \end{bmatrix} = \begin{bmatrix} 1 & 0 & \theta & 0 \\ 0 & 1 & 0 & \theta \\ -\theta & 0 & 1 & 0 \\ 0 & 0 & 0 & 1 \end{bmatrix} \begin{bmatrix} y_0 \\ y'_0 \\ z_0 \\ \delta_0 \end{bmatrix}. \quad (\text{A11})$$

Then we consider microbunches that are much smaller in  $z$  than  $y$  and neglect the  $R_{35}$  term. Thus we obtain an approximate expression for a thin bend:

$$R_\theta = \begin{bmatrix} 1 & 0 & 0 & 0 \\ 0 & 1 & 0 & \theta \\ -\theta & 0 & 1 & 0 \\ 0 & 0 & 0 & 1 \end{bmatrix}. \quad (\text{A12})$$

To get a thin offset quadrupole, we then just multiply the kick by a thin quadrupole matrix:

$$\begin{aligned} R_{Q\theta} &= R_\theta R_Q \\ &= \begin{bmatrix} 1 & 0 & 0 & 0 \\ 0 & 1 & 0 & \theta \\ -\theta & 0 & 1 & 0 \\ 0 & 0 & 0 & 1 \end{bmatrix} \begin{bmatrix} 1 & 0 & 0 & 0 \\ \frac{-1}{f} & 1 & 0 & 0 \\ 0 & 0 & 1 & 0 \\ 0 & 0 & 0 & 1 \end{bmatrix} \\ &= \begin{bmatrix} 1 & 0 & 0 & 0 \\ \frac{-1}{f} & 1 & 0 & \theta \\ -\theta & 0 & 1 & 0 \\ 0 & 0 & 0 & 1 \end{bmatrix}. \end{aligned} \quad (\text{A13})$$

### 3. Thick quad with instantaneous kick

We can also construct a matrix that treats the motion in the transverse plane as a thick quadrupole but treats the dipole kick as instantaneous. We repeat the procedure as done for Eq. (A13) but replace  $R_Q$  with two half-length thick quadrupoles. For angstrom-scale microbunches, it is

also important to consider the vacuum  $R_{56}$ ,  $\frac{l_Q}{\gamma^2}$ . For the focusing case, a half-quadrupole can be defined as

$$R_{Q_F/2} = \begin{bmatrix} \cos(kl_Q/2) & \frac{1}{k}\sin(kl_Q/2) & 0 & 0 \\ -k\sin(kl_Q/2) & \cos(kl_Q/2) & 0 & 0 \\ 0 & 0 & 1 & \frac{l_Q}{2\gamma^2} \\ 0 & 0 & 0 & 1 \end{bmatrix}. \quad (\text{A14})$$

We obtain

$$R_{Q_F\theta} = R_{Q_F/2}R_\theta R_{Q_F/2} = \begin{bmatrix} \cos(kl_Q) & \frac{1}{k}\sin(kl_Q) & 0 & \theta\sin(kl_Q/2) \\ -k\sin(kl_Q) & \cos(kl_Q) & 0 & \theta\cos(kl_Q/2) \\ -\theta\cos(kl_Q/2) & \frac{-\theta}{k}\sin(kl_Q/2) & 1 & \frac{l_Q}{\gamma^2} \\ 0 & 0 & 0 & 1 \end{bmatrix}. \quad (\text{A15})$$

We then consider a case where the kick angle is small, and the quadrupole is somewhat short, such that we can neglect terms of order  $\theta l_Q$  and higher. Applying the small angle approximation only to terms that contain  $\theta$  ( $\sin(kl_Q/2) \approx kl_Q/2$ ,  $\cos(kl_Q/2) \approx 1$ ), we then obtain a matrix for a thick quadrupole with an instantaneous kick. A similar process gives us the matrix for a defocusing quadrupole as well:

$$R_{Q_F\theta} = \begin{bmatrix} \cos(kl_Q) & \frac{1}{k}\sin(kl_Q) & 0 & 0 \\ -k\sin(kl_Q) & \cos(kl_Q) & 0 & \theta \\ -\theta & 0 & 1 & \frac{l_Q}{\gamma^2} \\ 0 & 0 & 0 & 1 \end{bmatrix} \\ R_{Q_D\theta} = \begin{bmatrix} \cosh(kl_Q) & \frac{1}{k}\sinh(kl_Q) & 0 & 0 \\ k\sinh(kl_Q) & \cosh(kl_Q) & 0 & \theta \\ -\theta & 0 & 1 & \frac{l_Q}{\gamma^2} \\ 0 & 0 & 0 & 1 \end{bmatrix}. \quad (\text{A16})$$

#### 4. Comparison

In this study, the quadrupole offsets used in the experiment were determined using the thick quad with instantaneous kick matrices. These matrices were simple enough that the quadrupole offsets could be solved analytically in MATLAB. While in principle, one could also solve for the quadrupole offsets analytically or numerically using the integrated function magnet, this is more computationally challenging.

Figure 11 shows that using the thick quad with instantaneous kick matrices may introduce a 1% error in the microbunch rotation tilt angle, compared with using the full integrated function magnet solution. The dashed lines show

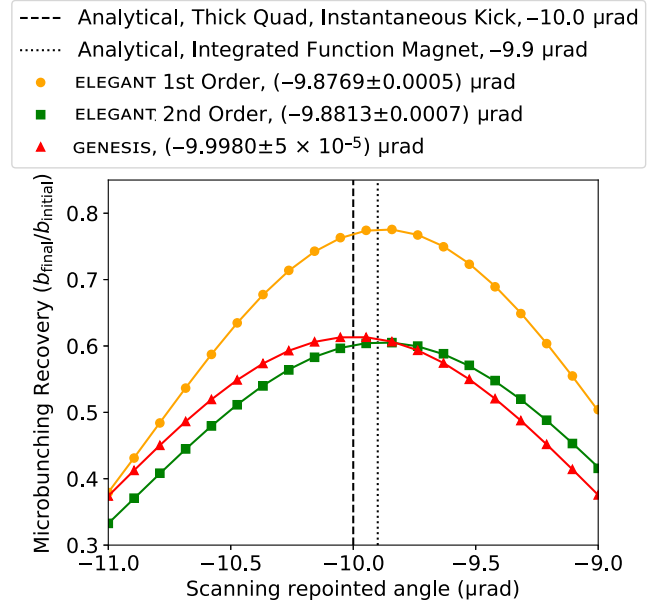


FIG. 11. Comparison of the optimal microbunch recovery angle determined using thick quad with instantaneous kick matrices, integrated function magnet matrices, ELEGANT, and GENESIS.

the microbunch tilt angle determined by the thick quad with instantaneous kick matrices ( $-10.0 \mu\text{rad}$ ) and the integrated function magnet matrices ( $-9.9 \mu\text{rad}$ ), using the experiment I offsets. Single Gaussian microbunch simulations were then performed in ELEGANT for both first and second-order matrices, and for GENESIS, using the experiment I offsets and parameters given in Table I. Then the microbunch tilt was determined by calculating the bunching factor at different angles and performing a Gaussian fit. Here we note that the “CSBEND” elements used for offset quadrupoles in ELEGANT produce a microbunch tilt angle that agrees well with integrated function magnet calculation, while the offset quadrupole elements in GENESIS agree with the thick quad with instantaneous kick calculation.

#### APPENDIX B: CALCULATION OF TRAJECTORY ANGLES

For the matrices in the main text theory section, the particle coordinates  $(y, y', z, \delta)$  rotate with the central particle trajectory as the beam experiences kicks such that  $z$  remains parallel and  $y$  remains normal to the particle trajectory. Thus before we can calculate the matrices that define our microbunch, we need to calculate the kick angles,  $\theta_1, \theta_2, \theta_3$ , provided by each offset quadrupole. We do this with a separate set of matrices where the particle coordinates in  $y$ ,  $\vec{y} = (y, y', 1)$ , do not rotate as the particle passes through a bend. As such, the quadrupole offsets,  $o_1, o_2$ , and  $o_3$  are defined as distances from the initial  $y$  axis and are not relative to the actual electron beam trajectory.

We consider a quadrupole with focal length  $f_1$ , which is offset in  $y$  by a distance  $o_1$ . The kick provided by a thin offset quadrupole is  $\theta = -\frac{1}{f}(y_0 - o_1)$ . When considering several kicks, it is convenient to use matrices to perform this calculation. To create a matrix  $M_{Q\theta 1}$  that can be used to find the trajectory following a thin offset quadrupole in  $(y, y', 1)$  phase space, we offset our incoming particle relative to the quadrupole center in  $y$  by  $-o_1$  using a matrix  $M_{-o_1}$ , perform quadrupole focusing using  $M_{Q1}$ , then undo the offset using  $M_{o_1}$ :

$$\begin{aligned} M_{Q\theta 1} &= M_{o_1} M_{Q1} M_{-o_1} \\ &= \begin{bmatrix} 1 & 0 & o_1 \\ 0 & 1 & 0 \\ 0 & 0 & 1 \end{bmatrix} \begin{bmatrix} 1 & 0 & 0 \\ \frac{-1}{f_1} & 1 & 0 \\ 0 & 0 & 1 \end{bmatrix} \begin{bmatrix} 1 & 0 & -o_1 \\ 0 & 1 & 0 \\ 0 & 0 & 1 \end{bmatrix} \\ &= \begin{bmatrix} 1 & 0 & 0 \\ \frac{-1}{f_1} & 1 & \frac{o_1}{f_1} \\ 0 & 0 & 1 \end{bmatrix}. \end{aligned} \quad (\text{B1})$$

This matrix produces the trajectory angle kick  $\theta_1$  for an on-axis particle ( $y_0 = 0$ ,  $y'_0 = 0$ ), through the first offset quadrupole in our triplet:

$$\begin{aligned} M_1 &= M_{Q\theta 1}, \\ \vec{y}_1 &= M_1 \vec{y}_0, \\ \begin{bmatrix} y_1 \\ y'_1 \\ 1 \end{bmatrix} &= \begin{bmatrix} 1 & 0 & 0 \\ \frac{-1}{f_1} & 1 & \frac{o_1}{f_1} \\ 0 & 0 & 1 \end{bmatrix} \begin{bmatrix} 0 \\ 0 \\ 1 \end{bmatrix}, \\ \theta_1 &= y'_1 = \frac{o_1}{f_1}. \end{aligned} \quad (\text{B2})$$

We can then find the trajectory angle following the second offset quadrupole by constructing a matrix of two offset quadrupoles and a drift, finding the angle after the second quadrupole, and then subtracting off the trajectory angle after the first quadrupole to find the kick angle of the second quadrupole:

$$\begin{aligned} M_2 &= M_{Q\theta 2} M_{L_1} M_{Q\theta 1} \\ &= \begin{bmatrix} 1 & 0 & 0 \\ \frac{-1}{f_2} & 1 & \frac{o_2}{f_2} \\ 0 & 0 & 1 \end{bmatrix} \begin{bmatrix} 1 & L_1 & 0 \\ 0 & 1 & 0 \\ 0 & 0 & 1 \end{bmatrix} \begin{bmatrix} 1 & 0 & 0 \\ \frac{-1}{f_1} & 1 & \frac{o_1}{f_1} \\ 0 & 0 & 1 \end{bmatrix} \\ \theta_2 &= y'_2 - y'_1 = \frac{1}{f_1 f_2} (f_1 o_2 - L_1 o_1). \end{aligned} \quad (\text{B3})$$

We repeat this procedure one more time to find the kick angle of the third quadrupole:

$$\begin{aligned} M_3 &= M_{Q\theta 3} M_{L_2} M_{Q\theta 2} M_{L_1} M_{Q\theta 1}, \\ \theta_3 &= y'_3 - y'_2 \\ &= -\frac{1}{f_1 f_2 f_3} (-f_1 f_2 o_3 + f_1 L_2 o_2 + f_2 L_2 o_1 \\ &\quad + f_2 L_1 o_1 - L_1 L_2 o_1). \end{aligned} \quad (\text{B4})$$

For the thick quadrupole case, we replace  $M_{Q1}$ ,  $M_{Q2}$ , and  $M_{Q3}$  with their thick quadrupole equivalents, e.g.,

$$\begin{aligned} M_{Q_D} &= \begin{bmatrix} \cosh(kl_Q) & \frac{1}{k} \sinh(kl_Q) & 0 \\ k \sinh(kl_Q) & \cosh(kl_Q) & 0 \\ 0 & 0 & 1 \end{bmatrix}, \\ M_{Q_F} &= \begin{bmatrix} \cos(kl_Q) & \frac{1}{k} \sin(kl_Q) & 0 \\ -k \sin(kl_Q) & \cos(kl_Q) & 0 \\ 0 & 0 & 1 \end{bmatrix}, \end{aligned} \quad (\text{B5})$$

and repeat the thin quadrupole procedure to find the trajectory kicks produced by thick quadrupoles.

### APPENDIX C: TAPER

Figure 12 shows the optimized undulator taper profiles following the  $K$  scans depicted in the main text. The 21 upstream undulators had a constant linear taper of  $\Delta K = -0.000185$  per undulator to compensate for wakefield energy losses. The nine reprinted undulators either continued this taper after an initial  $K$  detune or used a mild quadratic taper.

### APPENDIX D: ADDITIONAL GAIN CURVE MEASUREMENT

Figure 13 shows a gain curve of the final eight undulators, measured immediately before experiment I, with all 32 undulators lasing on-axis. We notice that the third to last undulator was performing suboptimally in that measurement, similar to its suboptimal performance in the gain curve in the microbunch rotation case.

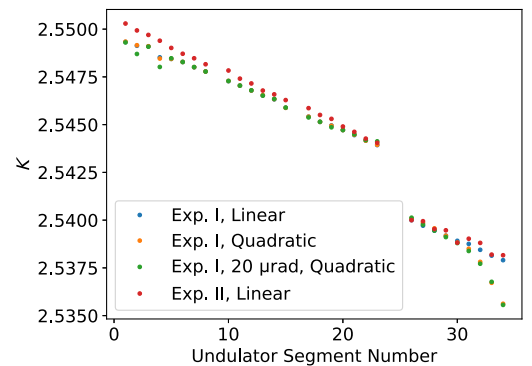


FIG. 12. Optimized undulator tapers for the four  $K$  scans shown in Fig. 7.

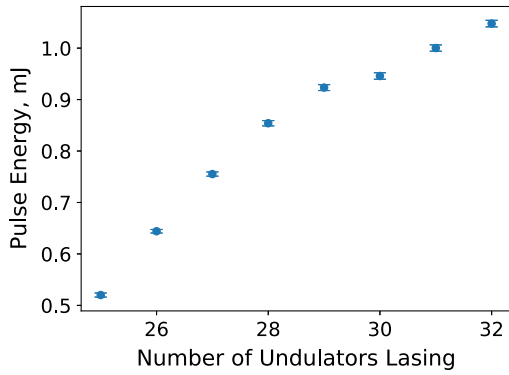


FIG. 13. Gain curve plotting the x-ray pulse energy in the last eight undulators with 32 LCLS HXU undulators lasing. Error bars give the standard error of the mean.

**APPENDIX E: ANGULAR SPOT SEPARATION**

Figure 14 shows the angle between the two spots during the gain curve taken in experiment I. Interestingly, the spot separation at the screen initially suggests microbunch lasing at 9  $\mu\text{rad}$ , which gain-guiding corrects to 10  $\mu\text{rad}$  after several undulators. This lower than expected initial angular separation may be due to suboptimal quadrupole offsets, which may have arisen due to an imprecise knowledge of beam parameters or the flattening of the orbit performed after the microbunch rotation triplet. Figure 15 shows the impact of the experimental electron beam energy differing from that which was used to determine the offset, and the impact of errors in the quadrupole offsets, using thick quad with instantaneous kick matrices and experiment I parameters.

Figure 15(a) indicates that using the wrong electron beam energy to determine the quadrupole offsets has a negligible effect on the electron beam trajectory and would require a  $> 400$  MeV (3.7%) error to produce a 1  $\mu\text{rad}$  error in the microbunch tilt angle. We expect the energy of the LCLS Cu linac at this energy is known to be at least 1%–2%, so an error in electron beam energy should not, on its own, explain the 1  $\mu\text{rad}$  error in separation which we observe.

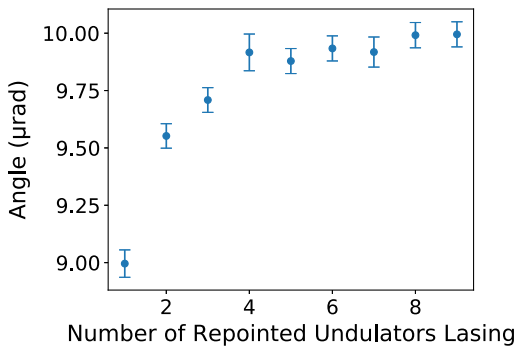


FIG. 14. Angular separation between the on-axis and rotated beams in Fig. 8. Error bars give the standard error of the mean, plus the error in screen calibration.

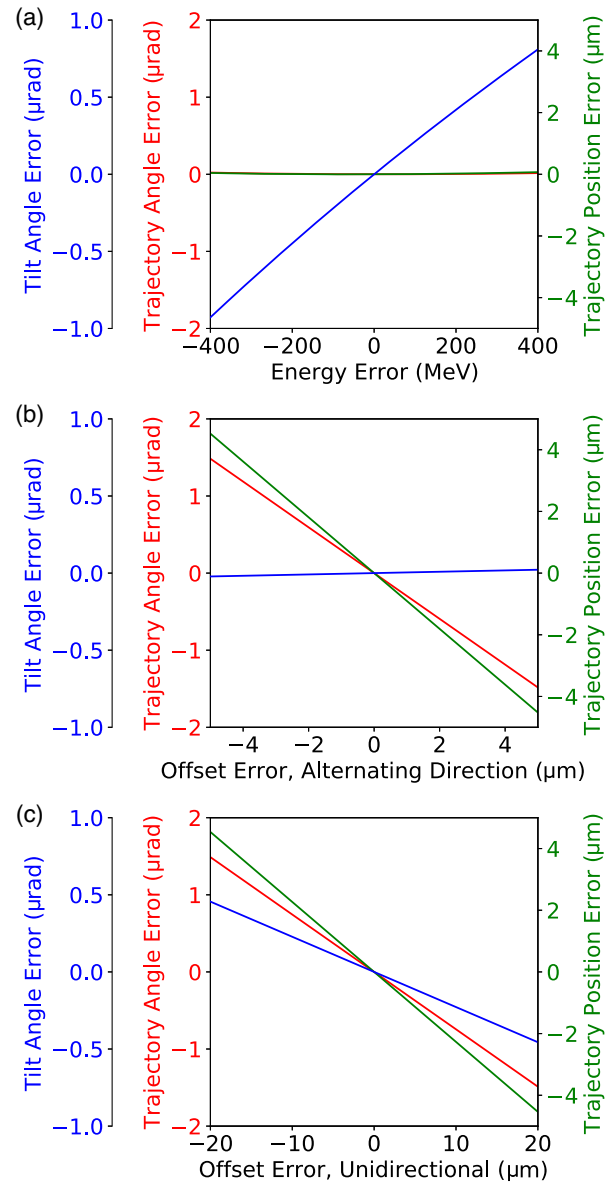


FIG. 15. Analytical calculation of the impact of errors in (a) electron beam energy, (b) alternating quadrupole offsets ( $o_1 + \text{err}$ ,  $o_2 - \text{err}$ ,  $o_3 + \text{err}$ ), and (c) uniform quadrupole offsets ( $o_1 + \text{err}$ ,  $o_2 + \text{err}$ ,  $o_3 + \text{err}$ ) for experiment 1 parameters.

Figure 15(b) shows that a few  $\mu\text{m}$  alternating errors in quadrupole offset ( $o_1 + \text{err}$ ,  $o_2 - \text{err}$ ,  $o_3 + \text{err}$ ) can cause microradian-scale errors in the trajectory angle. However, typically the quadrupole centers are known to better than 1  $\mu\text{m}$ , so this effect also should not, on its own, explain the 1  $\mu\text{rad}$  error in separation which we observe.

Figure 15(c) indicates that a few 10s of  $\mu\text{m}$  uniform error in quadrupole offset ( $o_1 + \text{err}$ ,  $o_2 + \text{err}$ ,  $o_3 + \text{err}$ ), such as may occur if the electron beam enters the triplet off-axis, can produce microradian-scale errors in both the microbunch tilt angle and trajectory angle. We used corrector magnets located between each of the nine downstream undulators to flatten the average trajectory to 10  $\mu\text{rad}$ ,

however, it is possible that the part of the beam that was lasing was offset with respect to the average beam, or it took a few correctors to fully correct to  $10 \mu\text{rad}$ . These scenarios may lead to the beam initially lasing with a trajectory or microbunch tilt angle  $1 \mu\text{rad}$  lower than expected.

## APPENDIX F: XTCAV MEASUREMENTS AND GENESIS SIMULATION DETAILS

Figure 16 shows x-ray transverse deflecting cavity (XTCAV) measurements that were taken prior to experiment I (a),(c) and experiment II (b),(d). Figure 16(a) has no undulators inserted, (b) is lasing at half power, and (c) and (d) are lasing at full power with 32 undulators inserted. The XTCAV measurements were used to determine the bunch length, current, and energy spread for comparison with simulation, as shown in (e)–(g). Slice central energy and RMS energy spread were determined by a Gaussian fit to each time bin in the XTCAV image. XTCAV voltage was 80 MV.

The electron beam distribution at the beginning of the undulator line was produced by ELEGANT. Figure 17 shows

the electron beam as input into GENESIS at the beginning of the undulator line for experiment I (a), (c) and experiment II (b), (d). The beam has been truncated in experiment II to have the same number of radiation wavelength slices as experiment I. To approximately match the electron beam lengths measured by XTCAV, we adjusted the bunch compression in the LCLS BC2 chicane [25] by making small modifications to the L2 phase, resulting in the energy- $z$  phase space shown in Figs. 17(a) and 17(b). To replicate the  $K$  detune we see in the experiment, we forced lasing on the tail by intentionally causing a tilt in the  $x$ - $z$  phase space. This was done by tweaking quadrupoles in a dispersive section of the LCLS BC2 chicane. These quadrupoles, which have a maximum integrated field gradient of  $\pm 2.1 \text{ kG}$  [26], are routinely used during the LCLS operations to flatten the  $x$ - $z$  phase space. Setting these quadrupoles to an integrated field of  $0.27 \text{ kG}$ , we can use them to intentionally tilt the  $x$ - $z$  phase space, as seen in Figs. 17(c) and 17(d). Figures 17(e)–17(g) show the current, slice central energy, and rms energy spread. These quantities were determined using GENESIS and represent the mean and standard deviation of each slice. Each GENESIS

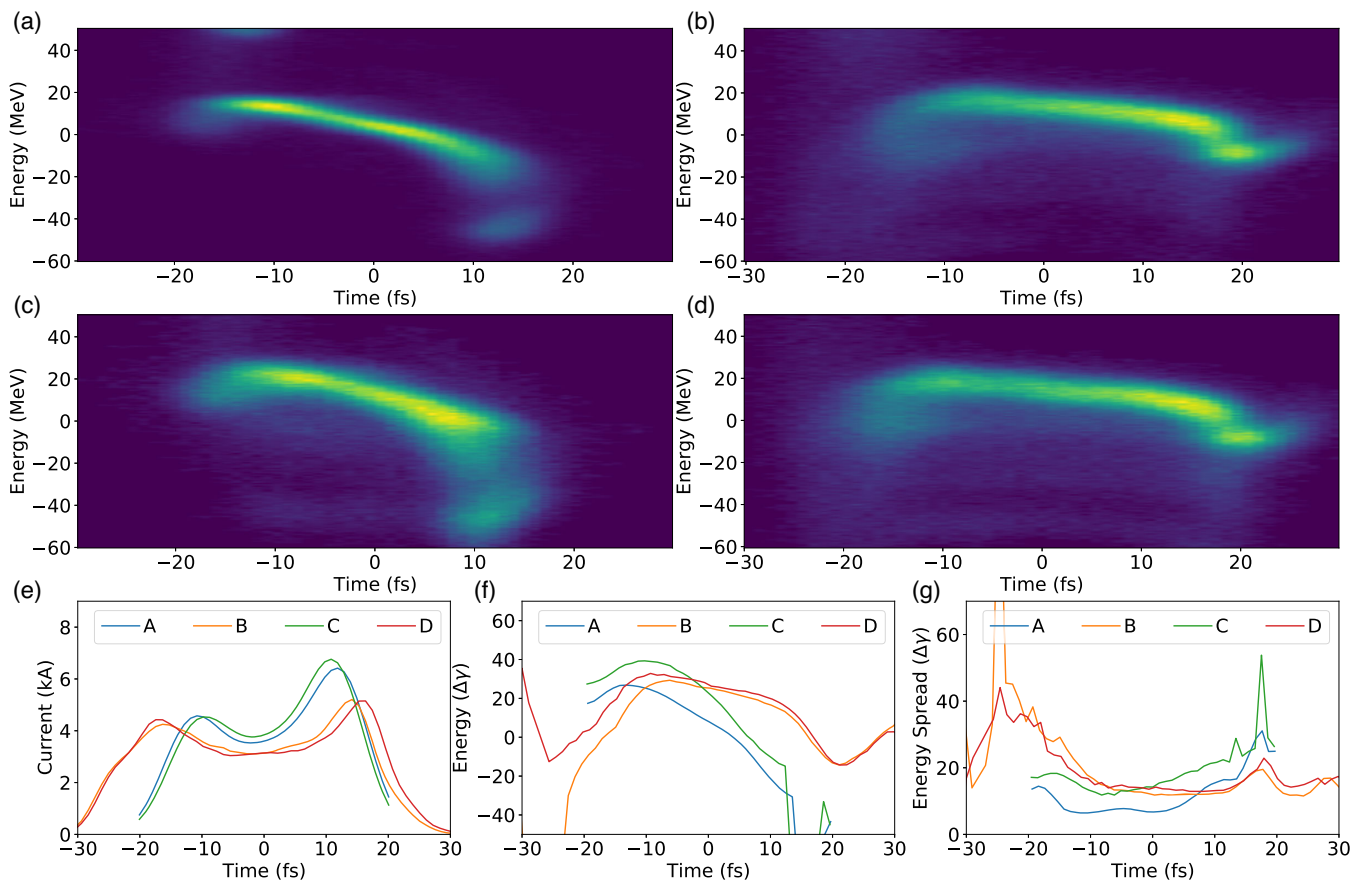


FIG. 16. XTCAV measurements at the end of LCLS-HXU. (a) Experiment I, no undulators inserted; (b) experiment II, lasing at half power; (c) experiment I, full power 32 on-axis undulator lasing; and (d) experiment II, full power 32 on-axis undulator lasing. (e)–(g) give the slice current, energy, and energy spread for the measurements in (a)–(d). Sign convention is head on left and tail on right.

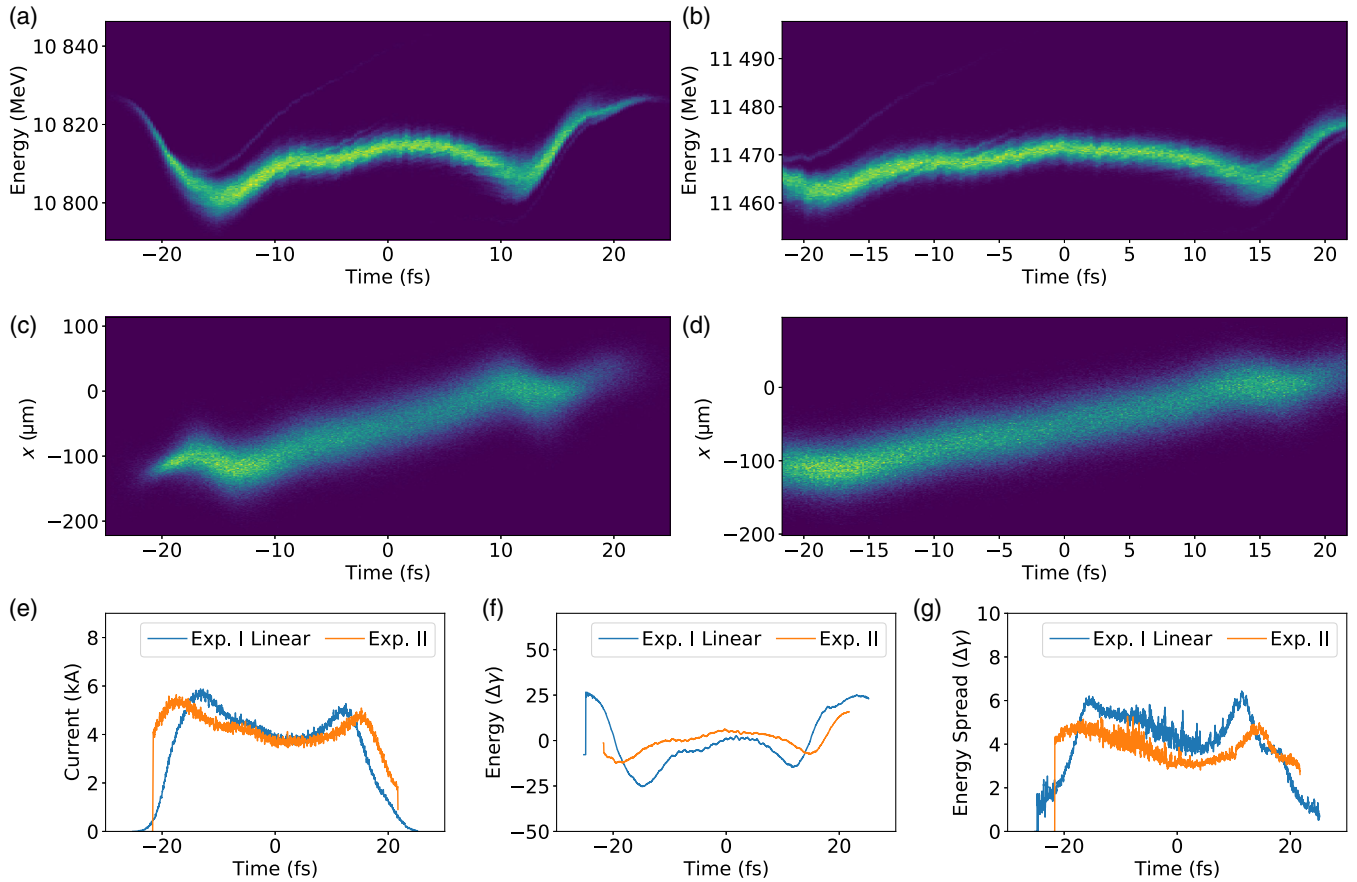


FIG. 17. Simulated beam from ELEGANT, as inserted into GENESIS at the beginning of the undulator line. (a)  $\gamma - t$  phase space for experiment I, (b)  $\gamma - t$  phase space for experiment II, (c)  $x - t$  phase space for experiment I, and (d)  $x - t$  phase space for experiment II. (e)–(g) give the slice current, energy, and energy spread for each simulation. Sign convention is head on left, tail on right.

simulation simulates every 30th radiation wavelength with 16 000 macroparticles per slice. We found a large number of macroparticles was necessary to suppress lasing off-axis [13].

We binned the electron beam into 100 bins and selected the appropriate electron bin to match the  $K$  detune observed in the experiment, which was the 67th bin from the head (experiment I) or 73rd bin from the head (experiment II). This bin was injected on axis, and the entire beam’s Twiss parameters ( $\beta_x, \alpha_x, \beta_y, \alpha_y$ ) were scaled to match this bin perfectly into the beam focusing lattice in GENESIS. Figure 18(a) shows the transverse profile of the electron beam and highlights how the tail of the beam was injected on axis.

We then scaled the electron beam emittance by a multiplicative factor to match the on-axis x-ray power. Figure 18(b) gives the slice emittance for experiment I (10  $\mu$ rad, linear taper) and experiment II. Table II gives the on-axis and reprinted spot powers measured in experiment and the corresponding powers in GENESIS for the four  $K$  scans shown in Fig. 7 (measured pulse energies are known to be within  $\sim 5\%$  error), as well as the emittance scaling factors.

Figures 18(c) and 18(d) show the x-ray power in the reprinted spot and electron beam bunching factor at the optimal  $K$ , showing that lasing in the electron beam head is suppressed. This is important, as Fig. 18(e) shows that the electron beam energy loss is larger in the tail than in the head. The electron beam energy loss simulated here comes from three factors: (i) spontaneous energy loss, (ii) resistive wall wakefields, and (iii) FEL lasing. Spontaneous energy loss occurs uniformly across the beam, but resistive wall wakefields cause increased energy loss in the electron beam tail, leading to the large, smooth features in Fig. 18(e). The high-frequency, sharp features in Fig. 18(e) show energy loss from FEL lasing. Wakefields used in GENESIS were externally calculated by a Green’s function method [27] using a function identical to that used for resistive-wall wakefields in LITRACK [28].

We can use this energy loss to predict the optimal  $K$  detune for lasing in each slice, after subtracting off a linear taper of 0.000185/undulator. Figure 18(f) shows this for the two  $K$  scans with linear taper. The dashed lines show the  $K$  detune found in the associated simulated  $K$  scan. We see that the optimal  $K$  detune is weighted toward the  $K$  detune of slices that undergo FEL lasing, while not aligning



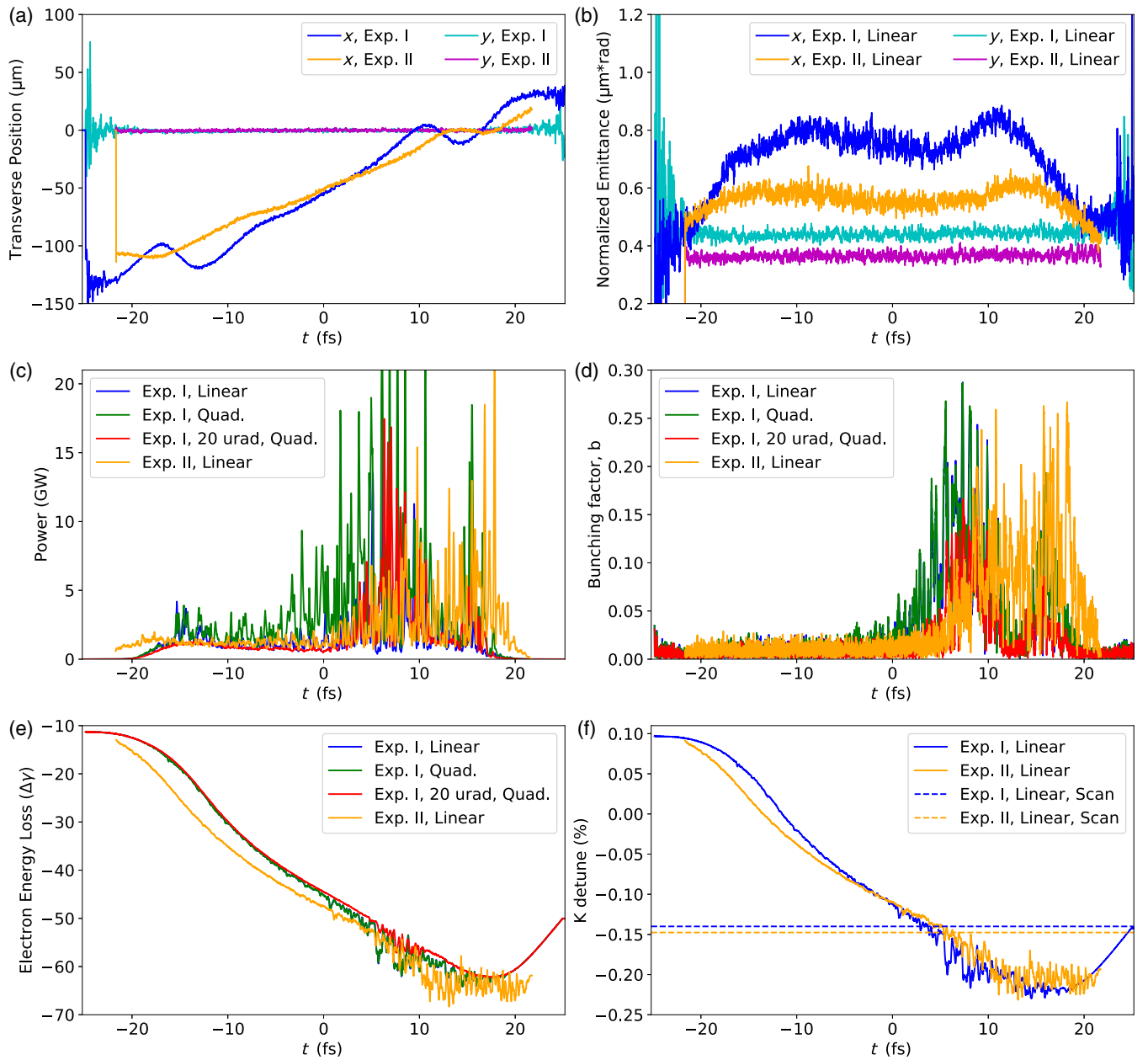


FIG. 18. Longitudinal profiles of simulations in Fig. 7. (a) Transverse position of beam at beginning of undulator line, (b) slice emittance at the beginning of the undulator line, (c) power after nine repointed undulators at optimal  $K$ , (d) bunching factor at the beginning of nine repointed undulators at optimal  $K$ , (e) electron energy loss comparing the beginning of the undulator line to the beginning of the repointed undulator line, and (f) predicted  $K$  detune based on energy loss, after subtracting a linear taper of 0.000185/undulator. Dashed lines give the  $K$  detunes found from the associated  $K$  scans. Sign convention is head on left and tail on right.

TABLE II. Pulse energy and scaling factors.

	Exp I, 10 $\mu$ rad, linear taper	Exp I, 10 $\mu$ rad, quadratic taper	Exp I, 20 $\mu$ rad	Exp II
Pulse energy, on-axis spot, Exp	120 $\mu$ J	116 $\mu$ J	31 $\mu$ J	168 $\mu$ J
Pulse energy, rotated spot, Exp	47 $\mu$ J	69 $\mu$ J	37 $\mu$ J	349 $\mu$ J
Pulse energy, on-axis spot, GENESIS	115 $\mu$ J	116 $\mu$ J	33 $\mu$ J	170 $\mu$ J
Pulse energy, rotated spot, GENESIS	109 $\mu$ J	140 $\mu$ J	69 $\mu$ J	94 $\mu$ J
Emittance scaling factor	1.223	1.215	1.695	1.065

perfectly with the center of the FEL lasing region due to a small amount of lasing in the head of the beam. This makes us confident that the increased energy loss due to lasing in the tail of the beam is what is causing the  $K$  detune in our GENESIS simulations.

Figure 19 serves to further reinforce the idea that lasing further on the tail of the beam makes the  $K$  detune more negative. Using an ELEGANT beam with experiment I parameters and a linear taper, we repeated the procedure

described above of selecting a longitudinal bin of the electron beam, placing that bin on axis and matching that bin to the undulator focusing lattice, then scanning the emittance to ensure 115  $\mu\text{J}$  in the on-axis spot. Figure 19(a) shows that performing this procedure with the 50th, 60th, and 70th bin of the beam changes the optimal  $K$  detune, as the beam lases progressively more on the tail of the beam, as evidenced by Figs. 19(b)–(e). Figure 19(f) shows that again, we can use the energy loss to predict the  $K$  detune of

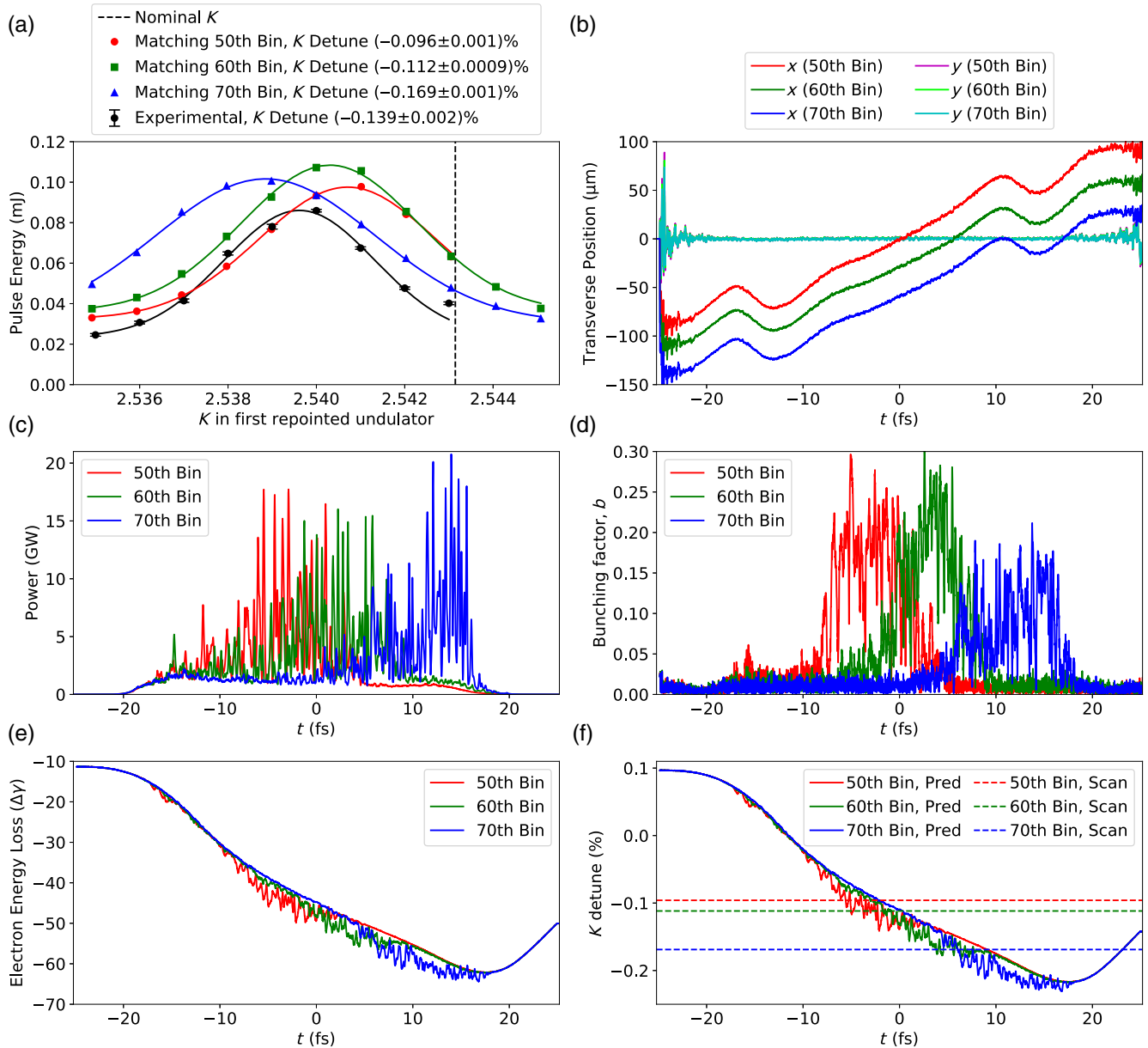


FIG. 19. Simulated demonstration of increased negative  $K$  detune on beam tail. The electron beam is divided into 100 bins, then simulations matching the 50th (red), 60th (green), and 70th (blue) bins are compared. (a)  $K$  scans with Gaussian fits, (b) transverse position of beam at beginning of undulator line, (c) power after nine reprinted undulators at optimal  $K$ , (d) bunching factor at beginning of nine reprinted undulators at optimal  $K$ , (e) electron energy loss comparing the beginning of the undulator line to the beginning of the reprinted undulator line, and (f) predicted  $K$  detune based on energy loss, after subtracting a linear taper of 0.000185/undulator. Dashed lines give the  $K$  detunes found from the associated  $K$  scans. Sign convention is head on left and tail on right. Errors in fit centers give the error of the Gaussian fit.

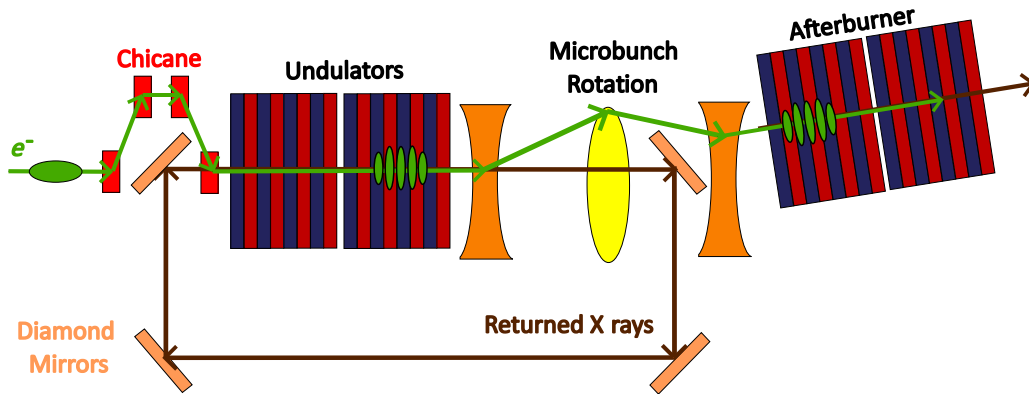


FIG. 20. A CBXFEL outcoupling scheme where the electron beam is sent around the cavity mirror, and microbunches are lased in an afterburner undulator section outside of the cavity.

each slice of the beam and find that the  $K$  detune of regions of the beam which lase approximately match the optimal  $K$  detune found in the  $K$  scan.

### APPENDIX G: CBXFEL OUT-COUPLING AROUND A MIRROR

In addition to the CBXFEL out-coupling method described in the text, where all undulators are enclosed within the cavity and x rays are outcoupled through a Bragg-reflecting mirror, one could also consider sending the electron beam around the cavity mirror, as depicted in Fig. 20. The microbunched electron beam could then be lased in undulators downstream of the cavity. The benefit of this scheme is that it allows for a smaller cavity with more relaxed alignment tolerances. The challenge of this scheme is achieving sufficient clearance between the cavity mirror and electron beam while still preserving microbunch rotation.

Figure 21 shows an example electron beam trajectory (using the parameters in Table I, experiment I,  $10 \mu\text{rad}$  rotation). Relative to the initial  $z$  axis, the electron beam  $y$  trajectory is  $-\frac{\alpha f_1 L}{4}$  in quadrupole 2, and  $\alpha L$  in quadrupole 3. The maximum orbit in the microbunch rotation triplet is

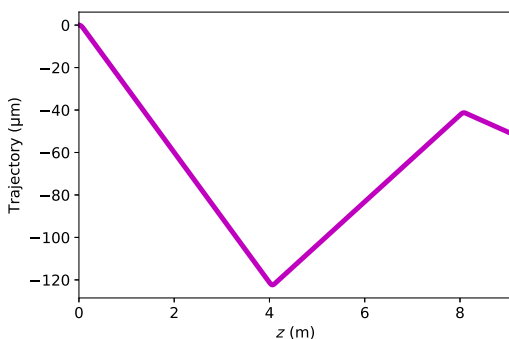


FIG. 21. A sample electron beam trajectory, calculated analytically using the parameters in Table I, experiment I,  $10 \mu\text{rad}$  rotation.

directly proportional to the microbunch rotation angle. For a  $40 \mu\text{rad}$  rotation,  $f_1 = -12 \text{ m}$  and  $L = 4.013 \text{ m}$ , this gives an orbit of  $482 \mu\text{m}$  in quadrupole 2, and  $160 \mu\text{m}$  in quadrupole 3. For a beam size of  $\sigma_y \approx 20\text{--}30 \mu\text{m}$ , this should provide sufficient clearance to send the electron beam around a cavity mirror. However, this is closer than thick diamond optics are typically brought to the electron beam at LCLS, and additional machine protection studies may be required. Additionally, as shown in the parameter scan in Fig. 4, a high microbunch rotation angle can reduce microbunching recovery significantly. One may either have to reduce the microbunch rotation angle, or out-couple the beam earlier in FEL gain, such that the electron beam energy spread is lower. One could also increase quadrupole strength, although this will also decrease the electron orbit in the microbunch rotation triplet.

- [1] N. G. Gavrilov, G. N. Kulipanov, V. N. Litvinenko, A. S. Sokolov, and N. A. Vinokurov, On mutual coherency of spontaneous radiation from two undulators separated by achromatic bend, *IEEE J. Quantum Electron.* **27**, 2566 (1991).
- [2] A. N. Matveenko, O. A. Shevchenko, and N. A. Vinokurov, Isochronous bend for high gain ring FEL, in *Proceedings of the 26th Free-Electron Laser Conference, Trieste, Italy, 2004* (Comitato Conferenze Elettra, Trieste, Italy, 2004).
- [3] Z. T. Zhao, Z. Wang, C. Feng, S. Chen, and L. Cao, Energy recovery linac based fully coherent light source, *Sci. Rep.* **11**, 23875 (2021).
- [4] D. F. Ratner and A. W. Chao, Steady-state microbunching in a storage ring for generating coherent radiation, *Phys. Rev. Lett.* **105**, 154801 (2010).
- [5] X. Deng, A. Chao, J. Feikes, A. Hoehl, W. Huang, R. Klein, A. Kruschinski, J. Li, A. Matveenko, Y. Petenev *et al.*, Experimental demonstration of the mechanism of steady-state microbunching, *Nature (London)* **590**, 576 (2021).

- [6] A. A. Lutman, J. P. MacArthur, M. Ilchen, A. O. Lindahl, J. Buck, R. N. Coffee, G. L. Dakovski, L. Dammann, Y. Ding, H. A. Dürr *et al.*, Polarization control in an x-ray free-electron laser, *Nat. Photonics*, **10**, 468 (2016).
- [7] J. P. MacArthur, A. A. Lutman, J. Krzywinski, and Z. Huang, Microbunch rotation and coherent undulator radiation from a kicked electron beam, *Phys. Rev. X* **8**, 041036 (2018).
- [8] Z. Huang and R. D. Ruth, Fully coherent x-ray pulses from a regenerative-amplifier free-electron laser, *Phys. Rev. Lett.* **96**, 144801 (2006).
- [9] G. Marcus, A. Halavanau, Z. Huang, J. Krzywinski, J. MacArthur, R. Margraf, T. Raubenheimer, and D. Zhu, Refractive guide switching a regenerative amplifier free-electron laser for high peak and average power hard x rays, *Phys. Rev. Lett.* **125**, 254801 (2020).
- [10] K.-J. Kim, Y. Shvyd'ko, and Sven Reiche, A proposal for an x-ray free-electron laser oscillator with an energy-recovery linac, *Phys. Rev. Lett.* **100**, 244802 (2008).
- [11] G. Marcus, J. W. J. Anton, L. Assoufid, F.-J. Decker, G. L. Gassner, K. Goetze, A. Halavanau, J. B. Hastings, Z. Huang, W. G. Jansma *et al.*, Cavity-based free-electron laser research and development: A Joint Argonne National Laboratory and SLAC National Laboratory Collaboration, in *Proceedings of the 39th International Free Electron Laser Conference, Hamburg, Germany* (JACoW, Geneva, Switzerland, 2019), pp. 282–287, <https://doi.org/10.18429/JACoW-FEL2019-TUD04>.
- [12] K.-J. Kim, L. Assoufid, F.-J. Decker, Z. Huang, R. R. Lindberg, G. Marcus, T. O. Raubenheimer, X. Shi, D. Shu, Y. Shvyd'ko *et al.*, Test of an x-ray cavity using double-bunches from the LCLS Cu-Linac, in *Proceedings of the 10th International Particle Accelerator Conference, IPAC-2019, Melbourne, Australia* (JACoW, Geneva, Switzerland, 2019), pp. 1887–1890, <https://doi.org/10.18429/JACoW-IPAC2019-TUPRB096>.
- [13] See Supplemental Material at <http://link.aps.org/supplemental/10.1103/PhysRevAccelBeams.27.030702> for figure source data, code that performs the matrix operations described in this text, and ELEGANT and GENESIS sample simulation input files.
- [14] M. Borland, ELEGANT: A flexible SDDS-compliant code for accelerator simulation, in *Proceedings of the 6th International Computational Accelerator Physics Conference, ICAP-2000, Darmstadt, Germany* (Advanced Photon Source, Lemont, IL, 2000), p. LS-287.
- [15] S. Reiche, GENESIS 1.3: A fully 3D time-dependent FEL simulation code, *Nucl. Instrum. Methods Phys. Res., Sect. A* **429**, 243 (1999).
- [16] S. Reiche, Update on the FEL code Genesis 1.3, in *Proceedings of the 36th International Free Electron Laser Conference, FEL-2014, Basel, Switzerland* (JACoW, Geneva, Switzerland, 2015), pp. 403–407.
- [17] LCLS-II Project Team, LCLS-II final design report, SLAC, Menlo Park, Technical Report No. LCLSII-1.1-DR-0251-R0, 2015.
- [18] C. Behrens, F.-J. Decker, Y. Ding, V. A. Dolgashev, J. Frisch, Z. Huang, P. Krejcik, H. Loos, A. Lutman, T. J. Maxwell *et al.*, Few-femtosecond time-resolved measurements of x-ray free-electron lasers, *Nat. Commun.* **5**, p. 3762 (2014).
- [19] N. Kroll, P. Morton, and M. Rosenbluth, Free-electron lasers with variable parameter wigglers, *IEEE J. Quantum Electron.* **17**, 1436 (1981).
- [20] Q. Jia, Analysis of emissions from prebunched electron beams, *Phys. Rev. Accel. Beams* **20**, 070702 (2017).
- [21] P. Rauer, A proof-of-principle cavity-based x-ray free-electron-laser demonstrator at the European XFEL, Ph.D. dissertation, Department of Physics, University of Hamburg, Hamburg, 2022, <http://dx.doi.org/10.3204/PUBDB-2022-02800>.
- [22] J. Duarte, R. Cassin, J. Huijts, B. Iwan, F. Fortuna, L. Delbecq, H. Chapman, M. Fajardo, M. Kovacev, W. Boutou, and H. Merdji, Computed stereo lensless x-ray imaging, *Nat. Photonics* **13**, 449 (2019).
- [23] D. Fainozzi, M. Ippoliti, F. Bille, D. De Angelis, L. Foglia, C. Masciovecchio, R. Mincigrucci, M. Pancaldi, E. Pedersoli, C. M. Günther *et al.*, Three-dimensional coherent diffraction snapshot imaging using extreme-ultraviolet radiation from a free electron laser, *Optica* **10**, 1053 (2023).
- [24] *Handbook of Accelerator Physics and Engineering*, edited by A. W. Chao and M. Tigner (World Scientific, River Edge, NJ, 1999).
- [25] K. L. F. Bane, F.-J. Decker, Y. Ding, D. Dowell, P. Emma, J. Frisch, Z. Huang, R. Iverson, C. Limborg-Deprey, H. Loos *et al.*, Measurements and modeling of coherent synchrotron radiation and its impact on the Linac Coherent Light Source electron beam, *Phys. Rev. ST Accel. Beams* **12**, 030704 (2009).
- [26] R. Carr, LCLS linac bunch compressor tweaker quadrupole magnets engineering specifications, SLAC, Menlo Park, Technical Report No. ESD-1.3-127-r0, 2005.
- [27] K. L. F. Bane and G. Stupakov, Resistive wall wakefield in the LCLS undulator beam pipe, SLAC, Menlo Park, Technical Report No. SLAC-PUB-10707, LCLS-TN-04-11, 2004.
- [28] K. L. F. Bane and P. Emma, LITRACK: A fast longitudinal phase space tracking code with graphical user interface, SLAC, Menlo Park, Technical Report No. SLAC-PUB-11035, 2005.

*Correction:* The omission of Supplemental Material has been rectified. A reference to the Supplemental Material and citations in text have been inserted.